Annual Report of 2008 Proposal (08013):

Proposal Title:	Seismic Documentation of Fault Cores and Damage Zones on the San Andreas Fault from Fault-Zone Guided Waves
Proposal Category:	Data Gathering and Products Integration and Theory
Science Objectives:	A7, A8, A10, and D
Disciplinary Activities:	Seismology, Fault and Rupture Mechanics
Interdisciplinary Focus Area:	Characterizing and Understanding Fault Damage and Healing on the San Andreas Fault over Multiple Length and Time Scales
Principal Investigators:	Yong-Gang Li at USC
Collaborative Investigators:	Elizabeth Cochran (UCR), Po Chen (UOW)
Funding Agent:	Southern California Earthquake Center.
Amount of Award:	**$**25,000
Date:	February 1, 2008 to January 31, 2009.

In our previous study at Parkfield San Andreas and the Calico fault in Eastern Mojave Desert, we have used the fault-zone trapped waves (FZTWs) generated by explosions and microearthquakes and recorded at the dense linear seismic arrays to characterize the near-fault crustal properties, including the fault-zone rock damage magnitude and extent, and healing process evaluated from measurements of seismic velocity changes caused by the mainshock. The damage magnitude and extent on the SAF inferred by FZTWs [*Li et al.*, 2004, 2006b] have been confirmed by the SAFOD mainhole drilling and logs. The progression of coseismic damage and postseismic healing observed at the Parkfield SAF is consistent with those observed at rupture zones of the Landers and Hector Mine earthquakes [*Li et al*., 2006a, 2007]. These results indicate that the greater damage was inflicted and thus greater healing is observed in regions with larger slips in the mainshock.

The present proposal is a continuing effort to determine the on- and off-fault damage at the San Andreas fault, Parkfield and the Calico fault using fault-zone guided waves. We used the fault FZTWs data recorded at the seismograph installed in the SAFOD mainhole at ~3 km depth where the borehole passed the SAF. The data include three-component waveforms from ~350 aftershocks of the 2004 *M*6 Parkfield earthquake. Many of aftershocks occurred at depths of 5 to 10 km so that the data allow us to document the rock damage on deep portion of the fault zone with high-resolution than those recorded at the surface array. We study the heterogeneities in geometry and material property of fault zones for further understanding the origin and mechanisms of fault damage and healing and their implications for stress heterogeneity and seismic hazard over multiple length and time scales in earthquake cycle. We study the contribution of on-fault damage to the total earthquake energy budget and the relationship between the damage magnitude and the absolute local stress level and stress drop. This proposal matches SCEC Science objectives A7, A10 and D3.

We also use the FZTWs (vertical incidence plane waves) recorded at our seismic array deployed at the Calico fault in 2006 for telemetry earthquakes to determine the fault-zone structure in the deep crust [*Cochran et al.*, 2008]. We integrate the data and results from FZTWs into physics-based models that will improve our understanding of earthquake phenomena, including to foster innovations of in deployments and to support one or more of the numbered SCEC science goals in A-D.

We have quantitatively determined the material properties of the fault core and damage zone and their variations with depth and along the strike on the SAF at Parkfield [*Li et al.*, 2008]. We are developing a computer code to invert the FZTW amplitudes to infer the properties of the velocity structure with a model that would be iteratively improved upon using the full 3D tomography (F3DT) [*Chen et al.*, 2007a, b] based on the scattering-integral (SI) method for fault-zone structure, in which the sensitivity (Fréchet) kernels are computed from the full physics of 3D wave propagation.

Papers an Conference Presentations Related to This Project:

Li, Y. G. and P. E. Malin, San Andreas Fault damage at SAFOD viewed with fault-guided waves, Geophys. Res. Lett., 35, L08304, doi:10.1029/2007GL032924 , 2008.

Li, Y. G., and P. Chen, Full-3D waveform tomography for the seismic velocity and attenuation structure on the San Andreas fault zone in Parkfield area, AGU Fall Meeting, December, S22A1322, 2008.

Li Y. G., P. E. Malin, E. S. Cochran, P. Chen, and J. E. Vidale, What we learned from fault-zone trapped waves at SAFOD after the 2004 *M*6 Parkfield earthquake, ICDP/SCEC Rapid Fault Drilling after Big Earthquakes Workshop, Tokyo, Japan, November 17-19, 2008.

Li, Y. G., J. E. Vidale, P. E. Malin, and E. S. Cochran, High-resolution imaging the internal structure and physical property of active faults at seismogenic depths by fault-zone trapped waves, "2008 BI-Lateral Workshop under the Sino-US Earthquake Studies Protocol" at Boulder, Colorado USA, May 20-23, 2008.

Li, Y. G., J. E. Vidale, E. S. Cochran, P. Chen, and Peter. E. Malin, Seismic documentation of rock damage and post-mainshock heal on the active faults ruptured during recent major earthquakes in California, "2008 BI-Lateral Workshop under the Sino-US Earthquake Studies Protocol" at Boulder, Colorado USA, May 20-23, 2008.

Li, Y. G., P. Chen, E. S. Cochran, and J. E. Vidale, Seismic velocity variations on the San Andreas Fault caused by the 2004 *M*6 Parkfield earthquake and their implications, Earth, Planets and Space, 59, 21-31,2007.

Li, Y. G., P. E. Malin and J. E. Vidale, Low-velocity damage zone on the San Andreas fault at depth near SAFOD site at Parkfield by fault-zone trapped waves, *Scientific Drilling*, Special Issue, No. 1, doi:10.2204 /iodp.sd.s01.09, 73-77, 2007.

Li, Y. G., P. Chen, E. S. Cochran, J. E., Vidale, and T. Burdette, Seismic evidence for rock damage and healing on the San Andreas fault associated with the 2004 *M*6 Parkfield earthquake, Special issue for Parkfield *M*6 earthquake, *Bull. Seism. Soc. Am.,* 96, No.4, S1-15, doi:10.1785/0120050803, 2006.

During the period (02/01/2007 – 01/31/2008) of this proposal, we have completed the proposed work:

We use the existing FZTW data recorded the surface array in our previous experiments at Parkfield combined with the data recorded at borehole seismometers in the SAFOD main hole [*Malin et al.*, 2006] to obtain a more detailed LVZ damage structure along with the strike and depth of the SAF. See Appendix I.

Appendix I. San Andreas Fault damage at SAFOD viewed with fault-guided waves

Yong-Gang Li
Department of Earth Sciences, University of Southern California, USA

Peter E. Malin
Institute of Earth Science and Engineering, University of Auckland, New Zealand

[1] Highly damaged rocks within the San Andreas fault zone at Parkfield form a low-velocity waveguide for seismic waves. Prominent fault-guided waves have been observed on the San Andreas Fault Observatory at Depth (SAFOD) seismographs, including a surface array placed across the fault-zone and a borehole unit placed in the SAFOD main hole at a depth of ~2.7 km below ground. The resulting observations are modeled here using 3-D finite-difference methods. To fit the amplitude, frequency, and travel-time characteristics of the data, the models require a downward tapering, 30-40-m wide fault-core embedded in a 100-200-m wide jacket. Compared with intact wall rocks, the core velocities are reduced by ~40% and jacket velocities by ~25%. Based on the depths of earthquakes generating guided-waves with long-duration wavetrains after the *S*-waves, we estimate that the low-velocity waveguide along the fault at the SAFOD site extends at least to depths of ~7 km. Thus it appears that significant damage zone exists at even twice the depths previously reported. *INDEX TERMs:* 7200 Seismology; 7209 Seismology: Earthquake dynamics and mechanics; 8123 Tectonophysics: Dynamics, seismotectonics. **Citation:** Li, Y.-G. and P. Malin (2007), San Andreas Fault damage at SAFOD viewed with fault-guided waves, *Geophys. Res. Lett.*, 35, L08304. Doi:xx/2007GL032924.

1. Introduction

[2] Field and laboratory studies indicate that fault zones appear to undergo high, fluctuating, stresses and pervasive cracking during earthquakes [*Mooney and Ginzburg*, 1986; *Chester et al.*, 1993; *Andrews*, 2005]. However, due in part to their depth of burial, the magnitude and spatial extent of the resulting rock damages are not well constrained [*Hickman and Evans*, 1992; *Sleep et al.*, 2000]. The thickness and depth of such zones are critical ingredients in the understanding of fault mechanics [*Dieterich*; 1978; *Scholz*, 1990; *Rice*, 1992]. This article discusses these characteristics as recently observed with special fault-guided wave recordings at the San Andreas Fault Observatory at Depth (SAFOD) site near Parkfield, CA.

[3] A zone of damaged rock surrounding the SAF at the SAFOD site has observed in previous studies using electromagnetic and seismic *P*- and *S*-wave travel time methods [*Unsworth et al*., 1997; *Thurber et al.*, 2003; *Roecker et al.*, 2004]. In these studies this zone is described as being a-little-as 200 hundred meters to as-much-as 1 km wide. The zone's observed seismic velocity reductions of 10-30% and *Vp/Vs* ratios approaching as-much-as 2.3 are thought to be caused by fracturing, brecciation, liquid-saturation, and high pore pressures. These features constitute a waveguide that traps seismic waves from earthquakes occurring within or close to it [*Li et al.*, 1990]. The amplitudes and dispersion feature of such trapped waves are known to be sensitive to the geometry and physical properties of the waveguide [*Li and Leary*, 1990; *Ben-Zion*, 1998]. At Parkfield, surface observations of fault-zone guided (trapped) waves suggest that a ~100-200-m zone of 20-40% *S*-wave velocity reduction exists to seismogenic depths [e.g. *Li et al.*, 1997, 2004a; *Malin et al.*, 1996; *Korneev et al.*, 2003]. Recently, SAFOD well logs from ~2.7 km underground have revealed a severely damaged zone around the San Andreas main fault characterized by highly fractured rock and multiple slip planes [*Hickman et al*., 2005]. This ~200 m wide zone consists of a 30-40 m central core of ~40% lower seismic velocities surrounded by a ~25% lower velocity jacket inferred by fault guided PSV waves recorded at the seismograph installed in the SAFOD main hole at depth [*Ellsworth and Malin*, 2006].

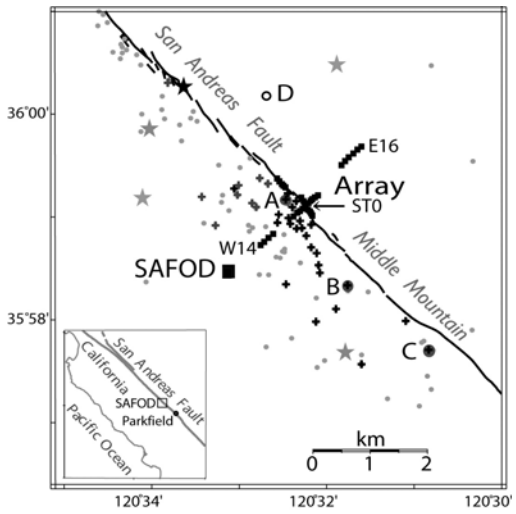

Figure 1 Locations of the study area (box in inset map), 45 portable seismographs (small squares) across and along the SAF near the SAFOD site (square), explosions (stars); and 120 microearthquakes (dots) recorded in the fall of 2003. Station ST0 of the array was located on the SAF surface trace; W14 and E16 on its west and east sides. Crosses denote 33 events generating fault-guided waves used in Fig. 4. Event A (solid circle), the SAFOD drilling target, occurred at ~2.7 km depth in 2003; its waveforms shown in Fig. 2c. Event B, a ~7 km deep aftershock of the 2004 *M*6 Parkfield earthquake, was recorded at the SAFOD main hole seismograph installed at ~2.7 km depth in 2005; its waveforms shown in Fig. 2d. Events C and D (solid and open circles) were deeper at 11 and 9 km, and were recorded on the surface array in 2003; their waveforms shown in Fig. 3.

2. Data and results

[4] In fall 2003, as part of a site characterization program, an array of 45 portable seismographs was deployed across and along the surface trace of the SAF

near SAFOD site [*Li et al.*, 2004b] (Fig. 1). About 120 local earthquakes were recorded at this surface array, including 33 events showing clear guide waves at depths between 2 and 12 km, from which the raypath incidence angles to ST0 are smaller than 30° from vertical. In December of 2004 and later a borehole seismograph was installed in the SAFOD mail hole at ~2.7 km depths where the SAF is characterized by a highly fractured and low velocity zone [*Ellsworth and Malin*, 2006] (Fig. 2a, b). Fig. 2c, d illustrate representative surface seismograms recorded at the surface array for a ~2.7 km-deep event (the SAFOD drilling target) in 2003 and borehole seismograms for a ~7 km-deep aftershock of the 2004 M6 Parkfield earthquake, showing the prominent fault guided waves which are simulated using the model in Fig. 2a.

[5] Figure 3 shows 3-component seismograms recorded at the surface array in 2003 for 2 other representative earthquakes: events C and D of Fig. 1. The primary focuses here on these events are their relative relationships in terms of event location and recording points versus the types of waves generated and what these imply for the velocity structure of the SAF at SAFOD. There are two major points to be made in this regard, both illustrated more details in Fig. 4. The first point to be made is that the events whose locations and observation points appear closest to the projected trace of the SAF generate prominent fault guided waves characterized by relatively large amplitudes and long wavetrains following *S*-waves. The second point is that the time dispersion of the latter signals after *S*-waves is a strong function of event depth. Taken together, these two characteristics imply that the guided waves were traveling along a relatively continuous channel connecting the events and observation points.

[6] These relations and the fault zone characteristics they imply were investigated further using a 3-D finite-difference waveform modeling code [*Graves*, 1996]. In this study, only the *S*-velocity related fault-zone trapped waves (FZTWs) were emphasized in the model computation. The study area was covered with a 10 m grid of computation

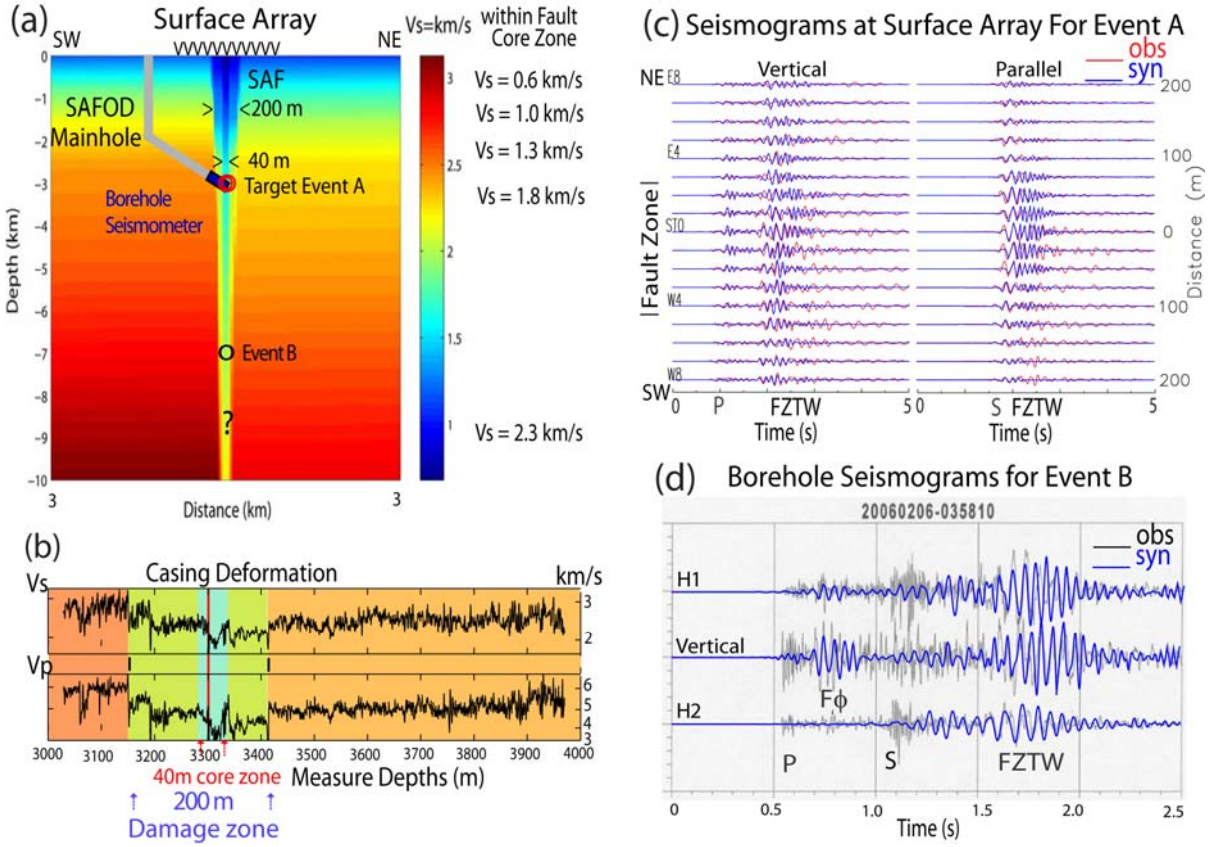

Figure 2 (a) Cross section near the SAFOD site showing the *S*-wave velocity model used in this study to compute synthetic fault-zone trapped waves (FZTWs) for the surface and borehole observations recorded in 2003 and 2005. Earthquakes A and B illustrate this type of fault guided waves used in this study. (b) Seismic velocities from SAFOD well logs showing the 40-m fault core and 200 m jacket low velocity damage zones [*Hickman et al.*, 2005]. The red line indicates the location where fault creep is deforming the borehole casing. (c) Observed (red) and computed (blue) vertical- and parallel-component seismograms at the surface array for event A. The seismograms were low-pass filtered below 8 Hz and are plotted using a single global scale. (d) Observed and computed 3-component borehole seismograms recorded for event B. The synthetic seismograms have been low pass filtered below 12 Hz. The large signal between the P- and S- waves labeled $\mathbf{F_\phi}$ has been recently identified as a fault guided P-wave [*Malin et al.*, 2006; *Ellsworth and Malin*, 2006].

point. A double-couple source is used for earthquakes while a point source used for explosions. The fault zone and surrounding rock velocity and attenuation in the model used for these simulations was built in several steps. First, the direct and guided waves from explosions shown in Fig. 1 were modeled to obtain a velocity model for the upper 2 km of the SAFOD site and the shallow structure of the SAF as we did for modeling the FZTWs recorded in our

previous experiment conducted near Parkfield [*Li et al.*, 2004a]. Then, using the well log velocities [*Hickman et al.*, 2005] and 2005 borehole seismogram [*Ellsworth and Malin*, 2006] as calibration points, progressively deeper earthquakes with prominent guided waves were modeled by adjusting the fault structure immediately above their hypocenters. The velocities in surrounding rocks are constrained by tomography profiles obtained at Parkfield [*Thurber et al.*, 2003; *Roecker et al.,* 2004]. The result of this process is the downward tapered, two-layer, low-velocity fault zone sandwiched between different east and west sides of the SAF (Fig. 2a.). The waveform fits corresponding to this velocity model are shown in Fig. 2c, d. The synthetic seismograms fit amplitude behaviors and traveltimes of the FZTWs recorded at both the borehole seismograph and surface array stations within the fault zone as well as those east and west of the SAF. They also fit the depth dependant dispersion characteristics of both the on-fault and off-fault source-receiver relations seen in the data (Fig. 4c). We tested a shallow fault zone truncated at 4 km depth in modeling for the 11 on-fault events. Fig. 4d illustrates the synthetic seismograms showing nearly the same wavetrain length of FZTWs after the *S*-waves for events below 4 km and shorter than those seen in Fig. 4c.

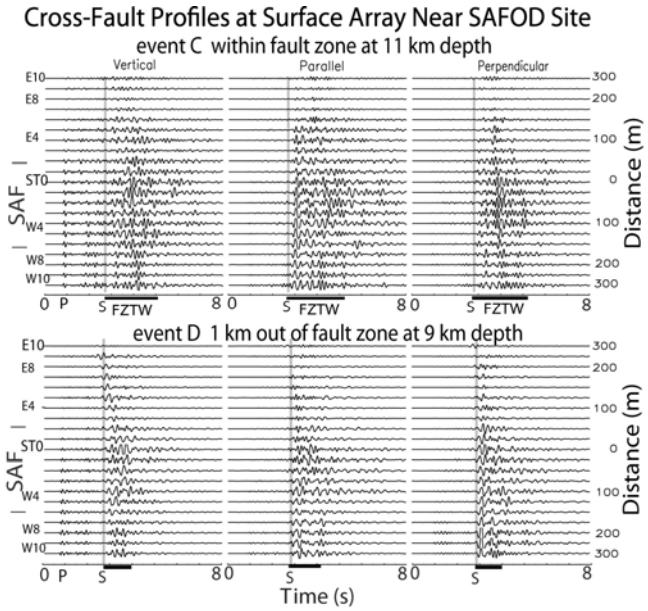

Figure 3 Three-component seismograms for events C and D. These representative seismograms were low-pass filtered below 6 Hz, aligned on the *S*-waves, and plotted with fixed amplitude scales for all traces in each plot. Fault-zone trapped waves (FZTW) with large amplitudes and long wavetrains after the S-arrivals are seen on the stations near the SAF surface trace at ST0 for the on-fault event C but not for the off-fault event D.

[7] Evidently, the SAFOD site guided waves can be explained in terms of a tapered, 30-40 m wide fault core of ~40% reduced velocity inside of a wider 100-200 m jacket of ~25% reduced velocity. The relatively intact rocks surrounding this composite damage zone have different velocities east and west of the SAF. Further, based on successful matching of the dispersion characteristics of the FZTWs following the *S*-waves as a function of depth, it would appear that, at least the low velocity jacket, and possibly its interior core, extends downward to no less than ~7 km (Fig. 4c). This is the depth inferred by the most clearly resolved and best fit guided waves seen in the SAFOD borehole seismograms [*Ellsworth and Malin*, 2006] that are modeled here (Fig. 2d).

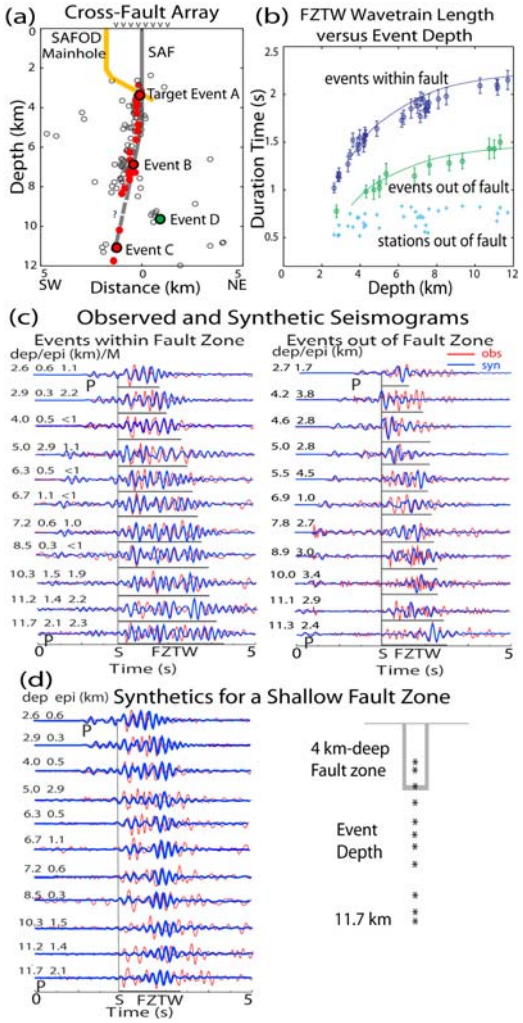

Figure 4 (a) Cross section through the SAF (grey line) at the SAFOD site showing locations of the microearthquakes (circles) with their epicenters shown in Fig. 1. Red circles mark 33 events showing strong fault-zone trapped waves (FZTW). Their epicenters are marked by crosses in Fig. 1. The locations of events A-D are also shown. (b) The measured time durations (denoted by blue circles) of FZTWs after *S* waves at stations within the fault zone for 33 on-fault earthquakes versus event depth, compared to those (green circles) measured at the same stations for off-fault earthquakes and those (blue crosses) at stations away from the fault zone for on- and off-fault events. Each data point is the average of 4 on- or off-fault stations. The error bars are standard deviations and the curves are polynomial fits to the data. (c) Observed and synthetic vertical-component seismograms at station ST0 for 11 on-fault and 11 off-fault earthquakes at different depths. *S*-arrivals for these events are aligned at the same time. The focal depth and epicentral distance from ST0 are plotted for each event. The finite-difference synthetic seismograms are computed using the model in Fig. 2a. Seismograms have been <8 Hz filtered and are plotted in trace-normalized. Bars denote the post-*S* wave durations, in which amplitude envelopes of FZTWs are above twice level in later coda. (d) Synthetic and observed seismograms at ST0 for 11 on-fault events using a 4-km-deep fault zone.

3. Discussions and Conclusions

[8] The damage zone at seismogenic depths may be caused by intense fracturing during earthquakes, including brecciation. Alternatively, given the fluid leakages currently taking place into the SAFOD well, the cause might relate to liquid-saturation and high pore-fluid pressure nears the fault. However, pore fluids arising from depth appear to hold a complex relationship with this damage zone, with its outer portions appearing to be more permeable than its core [Lockner et al., 2000]. Moreover, the damage zone may actually form more of a fluid barrier which fluids are simply pounded against. The damage zone is also asymmetric, apparently broader on the southwest side of the main fault trace. The asymmetry may imply that the fault has a moving damage zone or that when it ruptures it may preferentially damage the already weakened rocks [*Chester et al.*, 1993]. Alternately, greater damage may be inflicted in the extensional quadrant than the compressional quadrant near the propagating crack tip [*Andrews*, 2005]. Although the structural model shown in Fig. 2a accounts for the FZTWs and $\mathbf{F}_{\phi}$ observations and its parameters at ~3 km depth are confirmed by logging data, it is likely to represent a gross average of the actual fault-zone structure. The true structure in 3-D will certainly be more complicated, and the damage magnitude and extent will vary along the fault strike and depth due to rupture distributions and stress variations over multiple length and time scales.

[9] **Acknowledgments.** This study was supported by EarthScope Grant EAR0342277, USGS Grant NEHRP20060160, and the SCEC. The SCEC contribution number for this paper is 1128. Special thanks to S. Hickman, W. Ellsworth, and M. Zoback for their coordination, and J. Vidale, E. Cochran, E. Shalev, C. Thurber, S. Roecker, M. Rymer, R. Catchings, A. Snyder, L. Powell, B. Nadeau, N. Boness, and D. McPhee for their collaborations in our experiments at Parkfield.

References

Andrews, D. J. (2005), Rupture dynamics with energy loss outside the slip zone, *J. Geophys. Res., 110*, B01307, dio: 0.1029.

Ben-Zion, Y. (1998), Properties of seismic fault zone waves and their utility for imaging low-velocity structure, *J. Geophys. Res*., *103*, 12,567–12,585.

Chester F., Evans, J. and R. Biegel (1993), Internal structure and weakening mechanisms of the San Andreas fault, *J. Geophys. Res*., *98*, 771-786.

Dieterich, J. H. (1978), Time-dependent friction and the mechanics of strike-slip, *Pure Appl. Geophys*., *116*, 790-806.

Ellsworth, W. L., and P. E. Malin (2006), A first observation of fault guided PSV-waves at SAFOD and its implications for fault characteristics, *EOS, Transactions, and American Geophysics Union*, *87*, T23E-02, p154.

Graves, R. W. (1996), Simulating seismic wave propagation in 3D elastic media using staggered-grid finite differences, *Bull. Seism. Soc. Am*., *86*, 1091-1106.

Hickman, S. H., and B. Evans (1992), Growth of grain contacts in halite by solution-transfer: Implications for diagenesis, lithification, and strength recovery, in *Fault Mechanics and Transport Properties of Rocks*, pp. 253-280, Academic, San Diego, Cal.

Hickman, S. H., M. D. Zoback, and W. L. Ellsworth (2005), Structure and Composition of the San Andreas fault zone at Parkfield: Initial results from SAFOD Phase 1 and 2, *EOS, Transactions, and American Geophysics Union*, *83*, No.47, p237.

Korneev, V. A., R. M. Nadeau, and T. V. McEvilly (2003), Seismological studies at Parkfield IX: Fault-zone imaging using guided wave attenuation, *Bull. Seism. Soc. Am*. *80*, 1245-1271.

Li, Y. G., P. Leary, K. Aki, and P. Malin (1990), Seismic trapped modes in Oroville and San Andreas fault zones, *Science*, *249*, 763-766.

Li, Y. G. and P. C. Leary (1990), Fault zone trapped seismic waves, *Bull. Seism. Soc. Am.*, 80, 1245-1271.

Li, Y. G., W. Ellsworth, C. Thurber, P. Malin, and K. Aki (1997), Observations of fault-zone trapped waves excited by explosions at the San Andreas fault California, *Bull. Seism. Soc. Am. 87*, 210-221.

Li, Y. G., J. E. Vidale, and E. S. Cochran (2004a), Low-velocity damaged structure on the San Andreas fault at Parkfield from fault-zone trapped waves, *Geophys. Res. Lett. 31*, L12S06, p1-5.

Li, Y. G., E. S. Cochran, and J. E. Vidale (2004b), Low-velocity damaged structure on the San Andreas Fault at seismogenic depths near the SAFOD drilling site, Parkfield, CA from fault-zone trapped waves, *EOS, Transactions, and American Geophysics Union*, *85*, No. 47, F1313.

Lockner, D., H. Naka, H. Tanaka, H. Ito, and R. Ikeda (2000), Permeability and strength of core samples from the Nojima fault of the 1995 Kobe earthquake, *USGS Open file, Report* 00-129, 147-152.

Malin, P. E. M. Lou, and J. A. Rial (1996), $\mathbf{F_R}$ waves: A second fault-guided mode with implications for fault property studies, *Geophysical Research Letters, 23*, 3547 – 3550.

Malin, P. M., E. Shalev, H. Balven, and C. Lewis-Kenedi (2006), Structure of the San Andreas Fault at SAFOD from P-wave tomography and fault-guided wave mapping,, *Geophys. Res. Letter 33*, No. 13, pp. 13314, 2006GL025973.

Mooney, W. D. and A. Ginzburg (1986), Seismic measurements of the internal properties of fault zones, *Pure Appl. Geophys. 124*, 141-157.

Rice, J. R. (1992), Fault stress states, pore pressure distributions, and the weakness of the San Andreas fault, in *Fault Mechanics and Transport Properties of Rocks*, edited by B. Evans and T.-F. Wong, 475-503, Academic, San Diego, Calif.

Roecker, S., C. Thurber, and D. McPhee (2004), Joint inversion of gravity and arrival times data from Parkfield: New constraints on structure and hypocenter locations near the SAFOD drill site, *Geophys. Res. Lett., 31*, DOI 10.1029/2003GL019396.

Scholz, C. H. (1990), *The Mechanics of Earthquakes and Faulting*, Cambridge Univ. Press, New York.

Sleep, N. H., E., Richardson, and C. Marone (2000) Physics of friction and strain rate localization in synthetic fault gouge, *J. Geophys. Res. 105*, 25,875-25,890.

Thurber, C., S. Roecker, K. Roberts, M., Gold, L. Powell, and K., Rittger (2003), Earthquake location and 3-D fault zone structure along the creeping section of the San Andreas fault near Parkfield, CA: Preparing for SAF2OD, *Geophys. Res. Lett*. ***30***, 1112-1115.

Unsworth, M., P. Malin, G. Egbert, and J. Booker (1997), Internal structure of San Andreas fault at Parkfield, CA, *Geology*, 356-362.

Y.-G. Li, Department of Earth sciences, University of Southern California, Los Angeles, CA 90089, USA (ygli@usc.edu)

P.E. Malin, Institute of Earth Science and Engineering, The University of Auckland, Auckland, 1142, New Zealand (p.malin@auckland.ac.nz)

Appendix II. The Results from SAFOD Borehole Seismographs

In December of 2004 and afterwards, a seismograph was installed in the SAFOD mainhole at the ~3 km depths where the highly fractured and low velocity zone of the SAF was found in the SAFOD drilling and well logs [*Hickman et al.*, 2005]. A string of seismographs worked in the 1.2-km-deep pilot hole located at 1.8-km away from the mainhole at the same time. The borehole seismographs recorded ~350 aftershocks of the 2004 *M*6 Parkfield earthquake. Locations of these aftershocks are shown in Fig. 5. We have systematically examined the data recorded at the SAFOD borehole seismographs for the aftershocks in 4 groups with epicentral distances from the array: 1-2 km, 4-5 km, 8-10 km and 14-16 km, respectively (Fig. 5a).

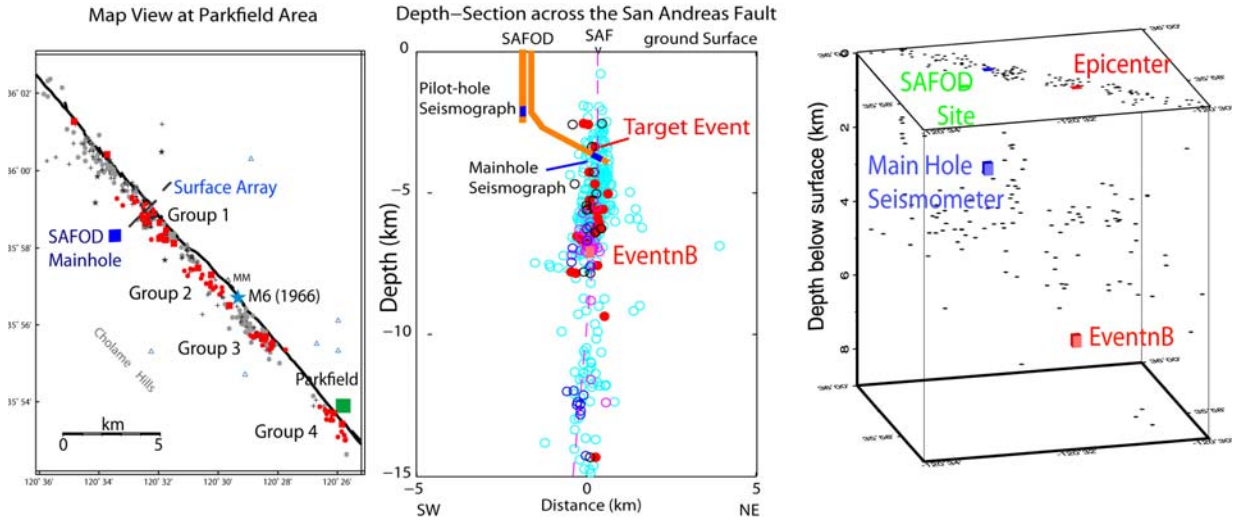

Fig. 5 (a) Left: Map view shows locations of ~350 aftershocks (circles) of the 2004 *M*6 Parkfield earthquake recorded at SAFOD borehole seismographs during December of 2004 and afterwards. Red circle denotes aftershocks in 4 groups at different epicentral distances to SAFOD site. The fault-zone trapped waves generated by these aftershocks are used in this study. The data recorded at the surface array (solid line across the fault) deployed in 2003 have been used in Appendix I. **Middle:** The vertical section across the SAF fault strike show locations of ~350 aftershocks (circles) recorded at SAFOD main-hole and pilot-hole seismographs. The fault-zone trapped waves generated by aftershocks in 4 groups denoted by red, black, pink and blue, respectively, are prominent in the SAFOD main-hole seismograms but not clear in the pilot-hole seismograms. **Right:** The 3-D view of locations of aftershocks (black dots)of the 2004 M6 Parkfield earthquake recorded at the SAFOD Main Hole seismograph (blue box). The red box denotes an example event which waveforms show the large secondary phases identified here as fault zone guided waves (see Fig. 2d in Appendix I). Waveforms recorded at the surface array for the target event and recorded at the SAFOD main-hole seismograph for Event B are shown in Fig. 2c of Appendix I.

For example, Fig. 6 shows seismograms recorded at the SAFOD borehole seismographs for 4 aftershocks in group G1 occurring at different depths of 3.8 km, 5.4 km, 7.9 km and 13 km within the fault zone. The prominent fault-zone trapped waves (FZTWs) with relatively large amplitudes at low frequency and long wavetrains arrived at the main-hole seismograph while pilot-hole seismograms show brief body waves at high frequency for the same events. We note that the length of FZTW wavetrains after the *S*-arrival increases with focal depths of these aftershocks, indicating that the low-velocity zone (damage zone) on the SAF extends to the depth of at least of ~8 km. Fig. 7 illustrates seismograms for 5 clustered aftershocks in group G4 occurring at depths of ~10.5 km within the fault zone, showing FZTWs dominant in the main-hole seismograms and but not in the pilot-hole seismograms. The FZTWs from the aftershocks in G4 at longer distances than those in G1 show longer wavetrains, indicating that the low-velocity waveguide (damage zone) on the SAF likely extends along the fault strike at least of ~20 km at seismogenic depths between the SAFOD site and Parkfield.

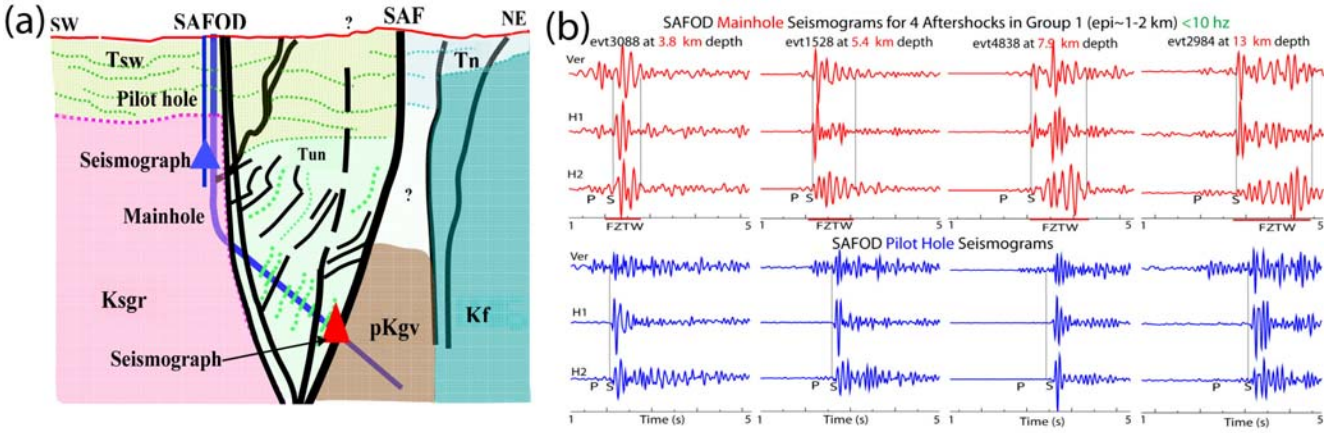

Fig. 6 (a) SW-NE cross section along the Phase 2 SAFOD main-hole toward the surface trace of the SAF. The borehole seismographs installed in the SAFOD main-hole and pilot-hole (denoted by red and blue triangles). The geological interpretation is based on the results of a Drill Bit Seismic reflection profile gathered during the 2004 Phase 1 drilling [*Ellsworth and Malin*, 2006]. **(b)** 3-component seismograms recorded at the SAFOD mainhole and pilot hole seismographs for 4 on-fault aftershocks in group G1 located at 1-2 km from the SAFOD site at different depths show prominent fault-zone trapped waves (FZTW) with large amplitudes and long wavetrains after *S*-waves at the mainhole seismograph. Seismograms are < 10 Hz filtered. The FZTWs from deeper events show longer time durations after S-arrivals than those from shallower events, indicating a low-velocity waveguide (damage zone) likely existing across seismogenic depths. Bottom: 3-component seismograms recorded at SAFOD mainhole and pilot hole seismographs for 5 on-fault clustered aftershocks of the 2004 *M*6 Parkfield earthquake show prominent fault-zone trapped waves (FZTW) with large amplitudes and long wavetrains after *S*-waves at the mainhole seismograph located within the fault zone but not at the pilot-hole seismograph 1.8 km away from the fault.

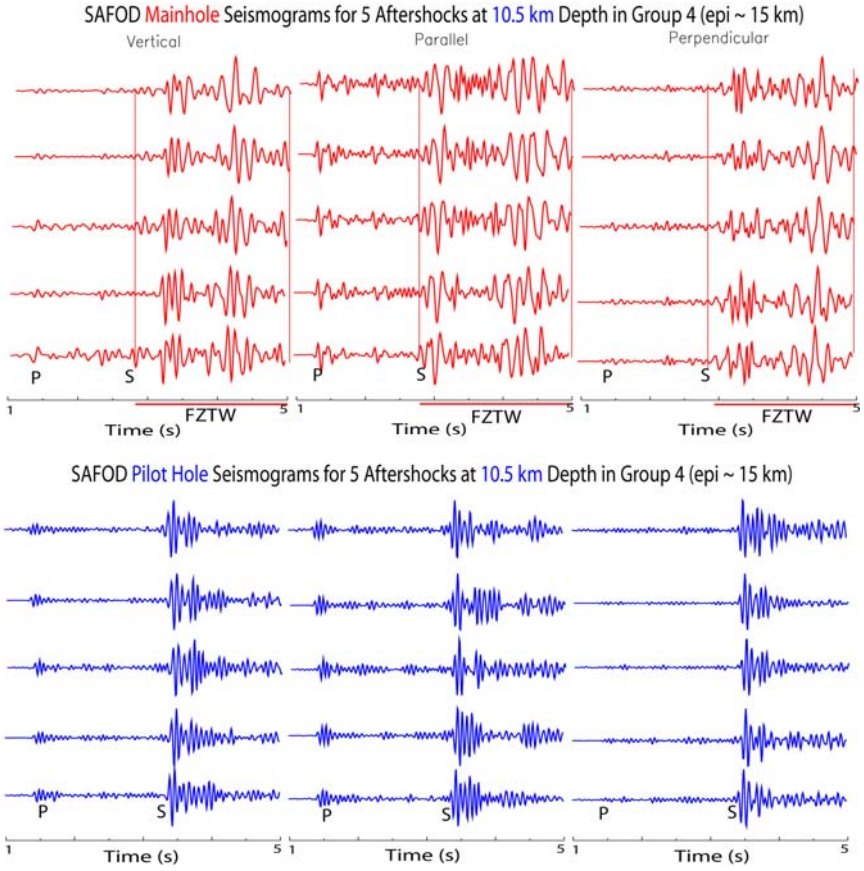

Fig. 7 3-component seismograms recorded at SAFOD mainhole and pilot hole seismographs for 5 repeated on-fault aftershocks in Group 4 of the 2004 *M*6 Parkfield earthquake show prominent fault-zone trapped waves (FZTW) with large amplitudes and long wavetrains after *S*-waves at the mainhole seismograph located within the fault zone but not at the pilot-hole seismograph 1.8 km away from the fault, indicating a low-velocity waveguide (damage zone) existing along the SAF strike and with depth. Bars indicate the time duration of FZTWs after *S*-arrivals. Note that the FZTW wavetrains from aftershocks in Group 4 with longer travel distances (~15 km) show longer time duration than those from aftershocks in Group 1 (1-2 km), indicating a continuous low-velocity waveguide (damage zone) along the fault strike and with the depth.

In order to examine the extension of the low-velocity zone along the SAF strike and with depth, we systematically measured the time duration of FZTW wavetrains after *S*-arrivals for aftershocks occurring at different depths and epicentral distances from the SAFOD site. For example, Fig. 8 shows waveforms for clustered aftershocks occurring within the fault zone at 4.4 km and 8.4 km depth, respectively, in group G2. The prominent FZTWs appear in mainhole seismograms but not in pilot-hole seismograms for the same events. Envelopes of seismograms show longer time duration of FZTWs in main-hole seismograms from the deeper aftershocks than those from the shallower events. The time durations of body waves in pilot-hole seismograms are much shorter than those in main-hole seismograms for the same aftershocks, and show no obvious changes in duration for the events at different depths. These observations show the existence of a low-velocity waveguide (damage zone) on the SAF at seismogenic depths.

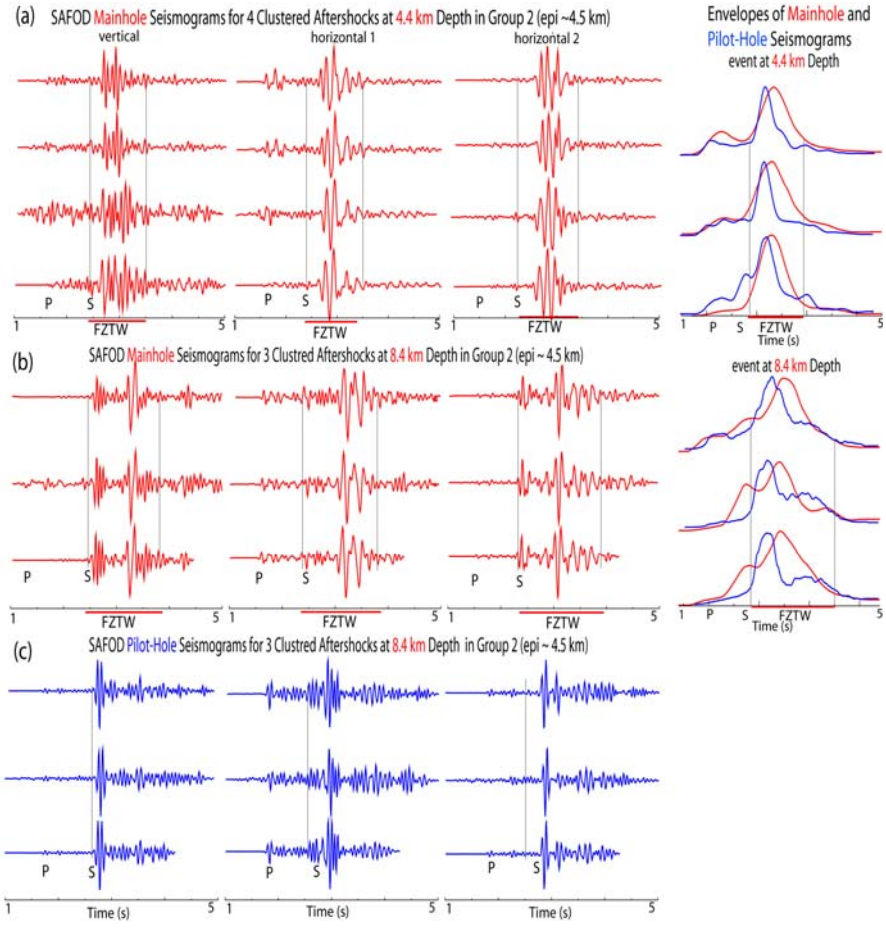

Fig. 8 (a) Left: 3-component SAFOD main-hole and pilot hole seismographs for 4 clustered on-fault aftershocks occurring at 4.4 km depth in group G2 show prominent fault-zone trapped waves (FZTW). Seismograms have been <10 Hz filtered. Right: Envelopes of main-hole (red lines) and pilot-hole (blue lines) seismograms for these clustered aftershocks. The horizontal bars denote the time duration of FZTW wavetrains after S waves, within which the amplitudes of FZTWS are at least twice higher than the amplitude of later coda waves. **(b)** The same as in (a) but for 3 clustered aftershocks occurring at 8.4 km depth in group G2 shows longer time durations of FZTWs than those from the events at the shallower depth in (a), indicating a low-velocity waveguide (damage zone) likely extending to deep seismogenic depths. Pilot-hole seismograms show a brief wavetrain with much short wavetrain than those in main-hole seismograms for the same events. **(c)** High-frequency body waves at relatively are dominant in the pilot-hole seismograms for the same aftershocks in (b).

More examples of SAFOD mainhole and pilot-hole seismograms for aftershocks within the fault zone at different depths in 4 groups G2-G4 with different distances from the SAFOD site are shown in Fig. 9, illuminating prominent FZTWs with large amplitudes and long wavetrains appearing in main-hole seismograms, but high-frequency body waves with brief wavetrains in pilot-hole seismograms for the same events. We note that the FZTWs from the aftershocks at longer hypocentral distances show longer wavetrains than those from short-distance events, indicating a continuous low-velocity waveguide (damage zone) extending along the SAF strike and with depth.

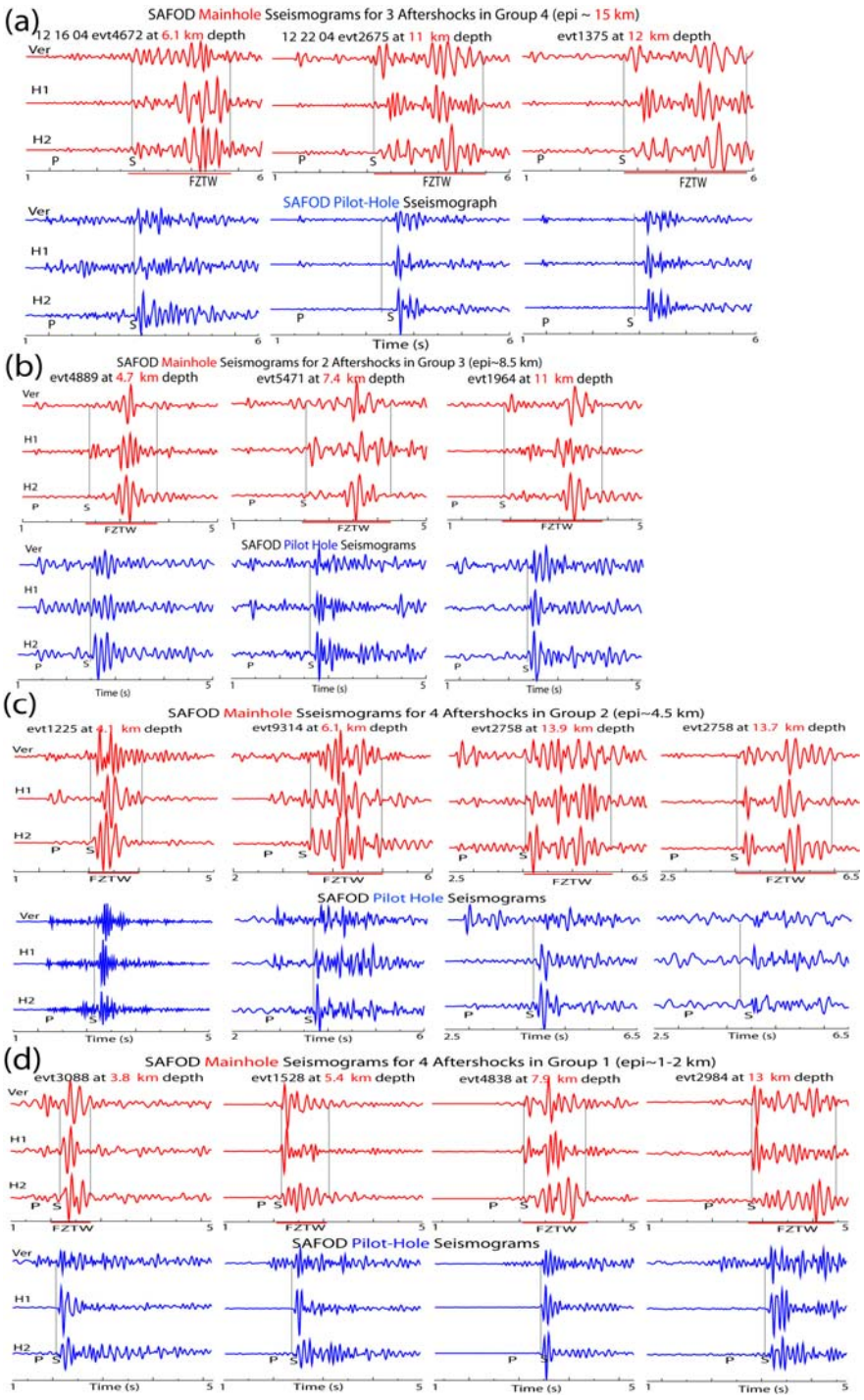

Fig. 9 (a) 3-component seismograms recorded at SAFOD mainhole and pilot hole seismographs for 3 on-fault aftershocks in group G4 with epicentral distances ~15 km from the SAFOD site at different depths show prominent fault-zone trapped waves (FZTW) with large amplitudes and long wavetrains after *S*-waves at the mainhole seismograph but not at the pilot-hole seismograms. Seismograms are < 10 Hz filtered. **(b)** 3-component main-hole and pilot-hole seismograms for 3 on-fault aftershocks in group G3 with epicentral distances of 8-10 km from the SAFOD site at different depths. **(c)** 3-component main-hole and pilot-hole seismograms for 4 on-fault aftershocks in group G2 with epicentral distances of 4-5 km from the SAFOD site at different depths. **(d)** 3-component main-hole and pilot-hole seismograms for 4 on-fault aftershocks in group G1 with epicentral distances <2 km from the SAFOD site at different depths. Note that FZTWs from deeper events show longer time durations after *S*-arrivals than those from shallower events, indicating a low-velocity waveguide (damage zone) likely across seismogenic depths. Also note that FZTWs from aftershocks in G4 at longer travel distances show the longer time duration after *S*-arrivals than those in G2 and G3 at the similar depths but shorter distances, indicating the low-velocity waveguide (damage zone) extending at least ~20 km continuously along the SAF strike at Parkfield.

In summary, Fig.10 shows measurements of time durations of FZTWs versus traveling distances from the aftershocks in groups G1-G4 (Fig. 10a) occurring within the fault zone. For example, Fig. 10b illustrates that the length of FZTWs wavetrains after *S*-waves in main-hole seismograms increases as the focal depth increases between 3.8 km and 13 km for 9 on-fault aftershocks in groups G1 and G2 with the epicentral distance less than ~4 km. In contrast, the body waves in pilot-hole seismograms show much shorter wavetrains after *S*-arrivals and flat changes with depths for the same events. The measured time durations of FZTWs from all 85 aftershocks in groups G1-G4 versus focal depth and epicentral distance show longer time durations of FZTWs after S-waves

as they travel over longer distances (Fig. 10c and Fig 10d). These observations illuminate that the low-velocity zone formed by damaged rockson the SAF likely extends along the fault strike at least of 15 km and to the depth at least of ~8 km at Parkfield.

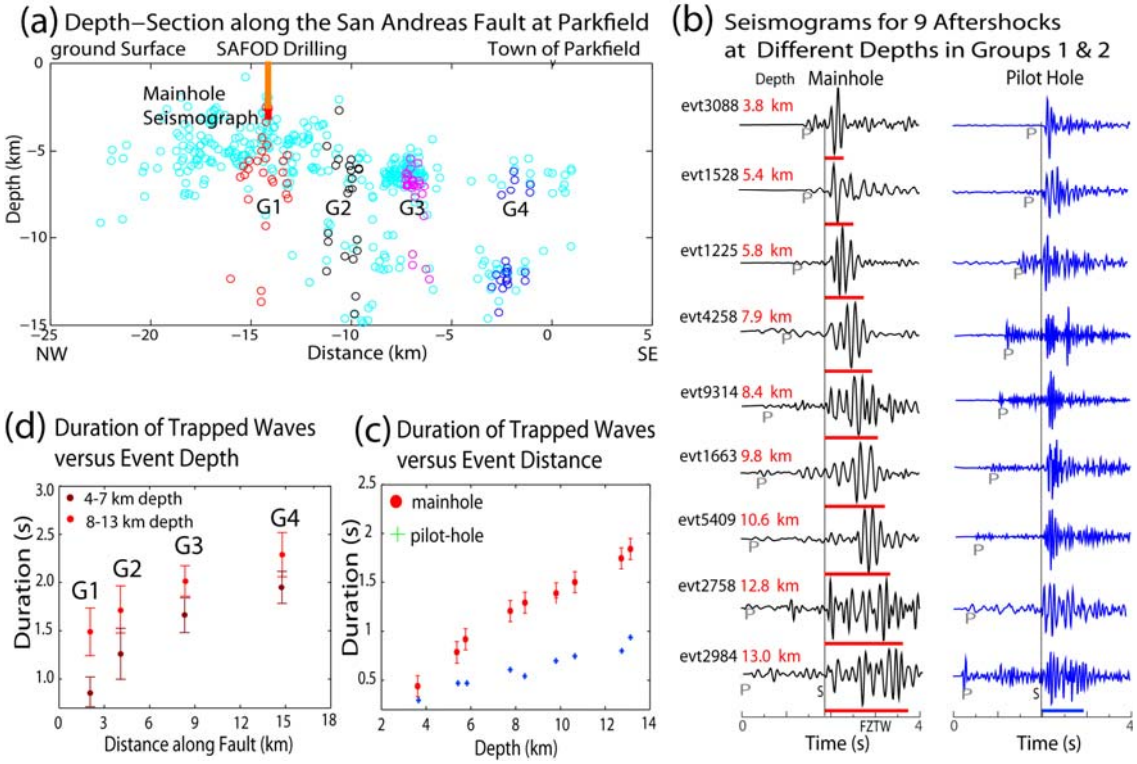

Fig. 10 (a) Vertical section along the SAF near the SAFOD site shows locations of ~350 aftershocks (circles) of the 2004 *M*6 Parkfield earthquake recorded at the borehole seismograph (red square) installed in the SAFOD main-hole at ~3 km depth. 80 aftershocks in 4 groups G1-G4 (denoted by red, black, pink and blue colors) at epicentral distances of ~1-2 km, 4-5 km, 8-9 km and 12-15 km from the SAFOD site, respectively, which show fault-zone trapped waves in main-hole seismograms. **(b)** Left: Vertical-component seismograms recorded at SAFOD mainhole seismograph for 9 on-fault aftershocks in group G1 and G2 at different depths show an increase in time duration (denoted by the red bar) of FZTWs as event depths increase. The incidence angles of raypaths from these events to the mainhole seismograph are smaller than 30^o to vertical. *S*-arrivals for these events are aligned at the same time. Right: Seismograms recorded at the SAFOD pilot-hole seismograph for the same events show much shorter FZTW wavetrains and flat changes with event depths. **(c)** The measured time durations of FZTWs after *S*-arrivals in mainhole (red) and pilot-hole (blue) seismograms versus focal depths for 9 on-fault aftershocks in (b). Each data point is averaged from measurements of 3 components for the events. Error bars are standard deviations. **(d)** The measured time durations of FZTWs after *S*-arrivals in mainhole seismograms for 80 aftershocks in 4 groups versus epicentral distances from SAFOD site. Each data point is averaged from measurements for aftershocks in each group. Red dots denote the measurements for events at depths of 4-7 km while violet dots denote the measurements for events at depths of 8-13 km. Error bars are standard deviations.

Based on our observations of fault-zone trapped waves, we construct a velocity and *Q* model across the SAF near the SAFOD site as shown in Fig. 11a. The model parameters at 3 km depth are constrained by direct measurements of the fault zone width and velocities in the SAFOD mainhole [*Hickman et al.*, 2005] (Fig. b). The wall-rock velocities are constrained by tomography profiles at Parkfield [*Thurber et al.*, 2004] (Fig. 11c). Using a 3-D FD code [*Graves*, 1996] in computation of synthetic seismograms. The study area is covered by a 3-D volume with 20-m spacing grids in computation. A double-couple source is used for earthquakes. We have simulated FZTW generated by explosions and shallow earthquakes recorded at the surface array to determine the shallow fault zone structure to ~3 km in our previous study of fault-zone trapped waves recorded at SAFOD site [*Li and Malin*, 2008]. Here, we simulated trapped waves from deep earthquakes recorded at the SAFOD

mainhole seismograph to obtain a model of the SAF with depth-variable structure at seismogenic depths. In order to fit the amplitude, frequency, and travel-time characteristics of the data, the models require a downward tapering, 30-40-m wide fault-core embedded in a 100-200-m wide jacket. Compared with intact wall rocks, the core velocities are reduced by ~40-50% and jacket velocities by ~25-35%. Based on the depths of earthquakes generating FZTWs with long-duration wavetrains after the *S*-waves, we estimate that the low-velocity waveguide along the fault at the SAFOD site extends at least to depths of ~7-8 km. For example, Fig. 11d illustrates 3-D finite-difference simulations of FZTWs recorded at the SAFOD mainhole seismograph for an aftershock occurring at 6.9 km within the fault zone.

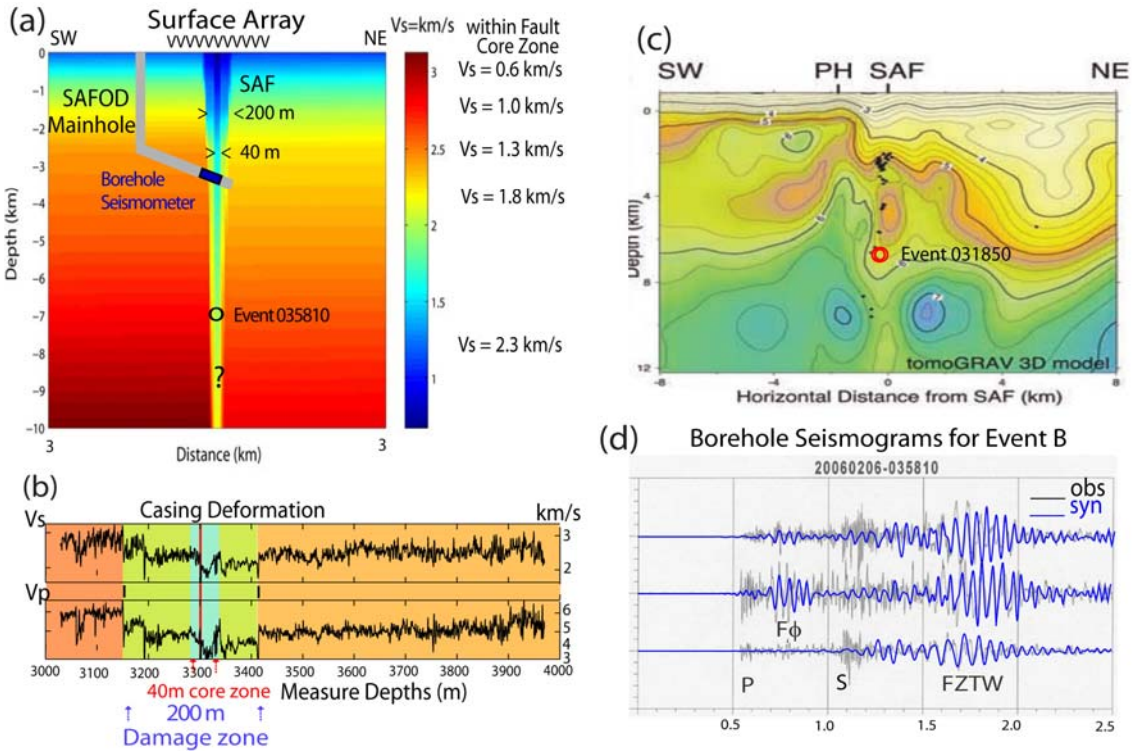

Fig. 11 (a) Cross section near the SAFOD site showing the *S*-wave velocity model used in this study to compute synthetic fault-zone trapped waves (FZTWs). The velocities within the 100-200-m wide waveguide on the SAF and surrounding rocks were found by 3-D finite-difference fits to the FZTWs generated by aftershocks at different depths. The model suggests that, on average, a fault zone consists of two vertical layers, a 30-40-m-wide fault core and a surrounding 100-200-m-wide damage zone. *S* velocities within the damage zone are reduced by 25-35% from wall-rock velocities. The maximum reduction occurs in the fault core and can be as large as 50%. The velocities of wall rocks are constrained by the results from 3-D tomography [Thurber et al., 2004; 2006]. **(b)** The velocities and width of the fault zone in (a) are consistent with the results from SAFOD drilling and logs, showing the 40-m fault core and 200 m jacket low velocity damage zones [*Hickman et al.*, 2004]. The red line indicates the location where fault creep is deforming the borehole casing. **(c)** The cross-section through the SAFOD site from the tomography DD 3D velocity model. Earthquakes within 1 km of the section are shown (filled circles), and the positions of the Pilot Hole (PH) and SAF trace (SAF) are indicated. Depths are relative to sea level. The 0.2 contour of the diagonal element of the model resolution matrix is shown in the result (dashed line). **(d)** Observed and synthetic three-component seismograms at the SAFOD main-hole seismograph for an aftershock occurring within the fault zone at depth 6.9 km. The synthetic seismograms have been low pass filtered below 12 Hz. The large signal between the *P*- and *S*-waves labeled $\mathbf{F_\phi}$ has been recently identified as a fault guided *P*-wave [*Malin et al.*, 2006; *Ellsworth and Malin*, 2006].

Through a thorough forward modeling procedure of fault-zone trapped waves generated by explosions and earthquakes occurring at different depths and epicentral distances, we obtained best-fit model parameters. Figures 12-15 show the 3-D FD synthetic waveforms from aftershocks in groups G1-G4 to fit FZTWs recorded at the SAFOD main-hole seismograph.

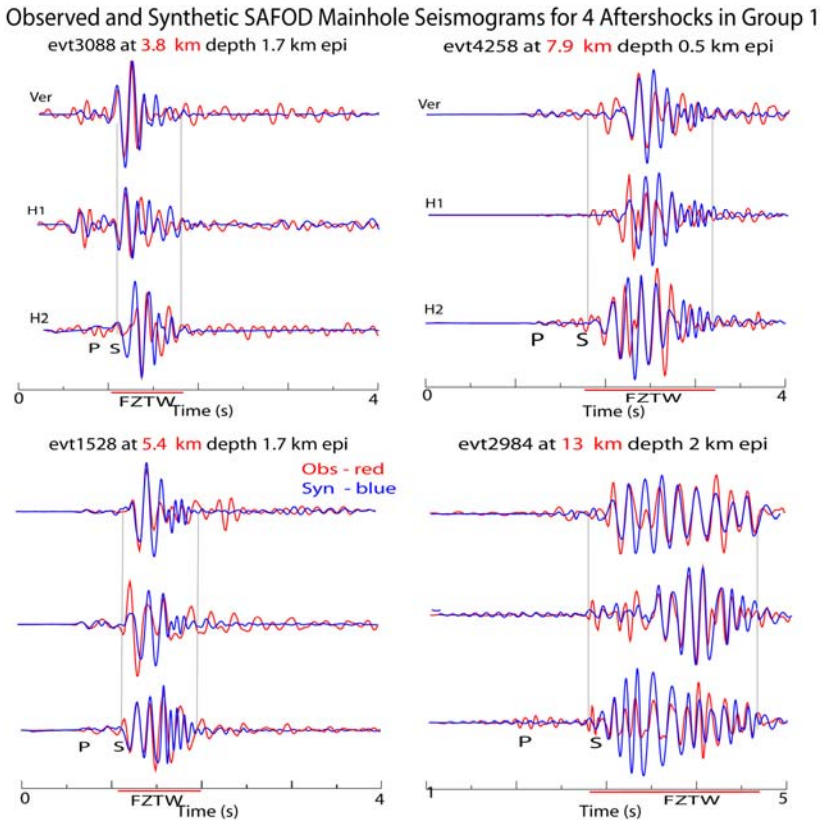

Fig. 12 Observed and 3-D finite-difference seismograms at SAFOD mainhole seismograph for 4 Parkfield aftershocks in group G1 at 1-2-km epicentral distances and different depths within the fault zone show prominent fault-zone trapped waves (FZTWs). The model in Fig. 11a is used for FD waveform computation. The fault zone extends to 13-km depth. A double-couple source is used for aftershocks located at certain depths within the fault zone. The raypaths from these aftershocks to the main-hole seismograph are nearly vertical. The time duration of FZTWs after S-arrivals are 0.75 s, 1.1 s, 1.5 s and 2.0 s for the events at depths of 3.8 km, 5.4 km, 7.9 km and 13 km, respectively, showing that the low-velocity damage zone on the SAF likely extends across seismogenic depths although the velocity reduction within the deeper portion of the fault zone is smaller that those at shallower depth.

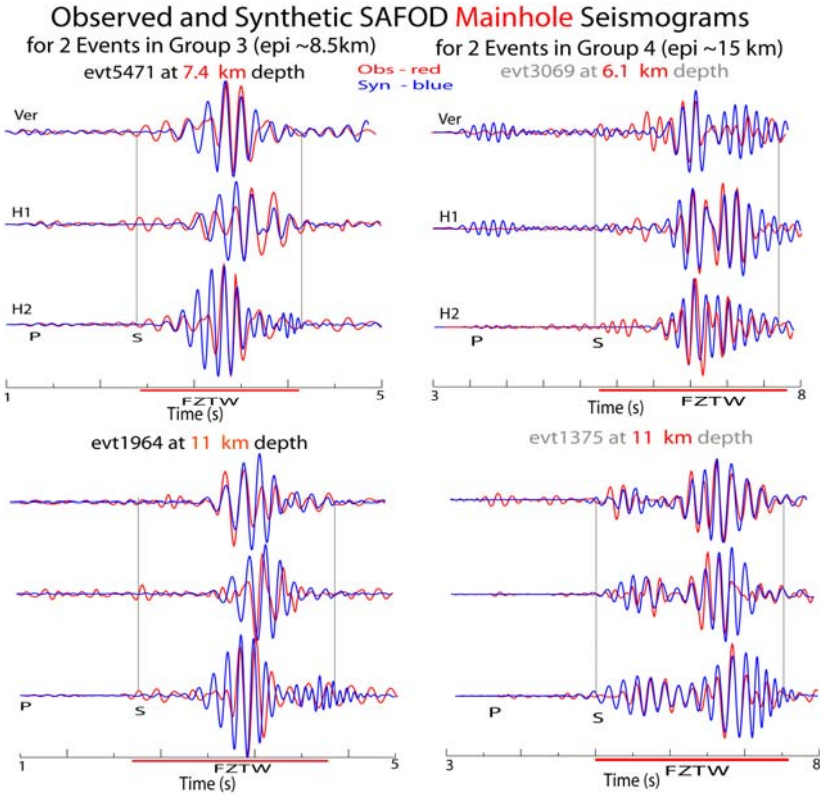

Fig.13 Observed and 3-D finite-difference seismograms at SAFOD mainhole seismograph for (Left) 2 Parkfield aftershocks in group G3 at epicentral distances of 8-9 km and (Right) other 2 aftershocks in group G4 at epicentral distances of 12-15 km occurring at different depths within the fault zone show that the longer time durations of FZTW wavetrains after *S*-arrivals as they travel over a longer distance along the fault strike and with the depth, suggesting a continuous low-velocity waveguide formed by the damaged rock on the SAF extending across seismogenic depths. Other notations are the same in Fig. 12.

We have tested the model including the low-velocity fault zone truncated at various depths to examine the depth extension of the damage zone on the SAF at SAFOD. For example, we obtain a good fit of synthetic waveforms computed using the model with a deep fault zone in Fig. 11a to observed FZTWs with long wavetrains recorded at the SAFOD mainhole seismograph for two aftershocks occurring at depths of 8.4 km and 10.6 km (Fig. 14a). However, the synthetic FZTWs using the model with a shallow fault zone truncated at the depth of 4 km show much shorter wavetrains after *S*-arrivals, which can not match the long wavetrains of observed FZTWs. We suggest the low-velocity waveguide (damage zone) on the SAF near the SAFOD site likely extends to the depth of at least ~8 km.

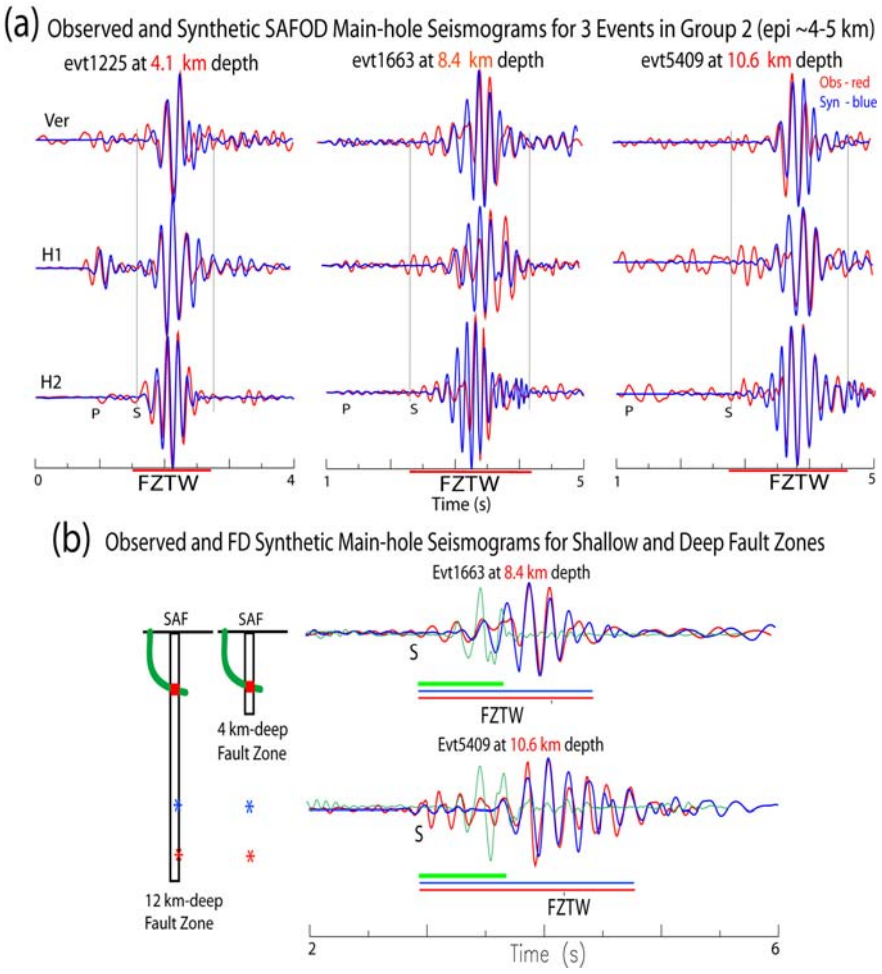

Fig. 14 (a) 3-D finite-difference seismograms using the model in Fig. 11a fit SAFOD main-hole seismograms for 3 on-fault aftershocks in group G2 with epicentral distances of 4-5 km at different depths within the fault zone show prominent FZTWs, the wavetrain length of which increase as the travel distance increases. Seismograms have been filtered (<6 Hz). **(b)** Observed and 3-D finite-difference main-hole seismograms for 2 Parkfield aftershocks in group G2 occurring at depths of 8.4 km and 10.5 km within the fault zone. The computed seismograms (blue lines) using a deep low-velocity fault zone extending to 12 km depth are agreeable with observed seismograms (red lines) characterized by the long duration of FZTWs after S-waves. In contrast, the computed seismograms (green lines) using a shallow fault zone truncated at 4 km depth show shorter FZTW wavetrains that can not match observations. This test manifests that the low-velocity waveguide (damage zone) on the SAF at Parkfield extends to the deep potion of seismogenic depths.

Finally, we computed finite-difference synthetic waveforms using the model in Fig. 11a to fit seismograms recorded at the surface seismic array deployed in 2003 [*Li and Malin*, 2008]. For example, Fig. 15 shows FD simulations of FZTWs for explosion SP20 detonated within the fault zone at ~3 km north of the SAFOD site and 3 on-fault micro-earthquakes at depths of 3 km, 6.9 km, and 11 km, respectively. The earthquake at 3 km is a SAFOD target event with *M*2.3 occurring on the Julian Date R293 in 2003. Synthetic FZTWs for the earthquake occurring at 6.9 km depth show longer wavetrains after *S*-arrivals than those for the target event at 3 km depth while the FZTWs for the deep earthquake at 11 km depth show the longest wavetrains. The synthetic FZTW waveforms are agreeable with observations. In the modeling procedure, we tested finite-difference simulations for a deep earthquake located at the depth of 11 km using the model with a low-velocity waveguide

at the depth shallower than 5 km. The synthetic seismograms using this testing model show FZTWs with much shorter wavetrains after *S*-arrivals, which could not match the long wavetrains of FZTWs observed for this deep event. The results from these simulations of FZTWs indicate our model with a deep low-velocity fault zone shown in Fig. 11a is applicable for the structure of the San Andreas fault at seismogenic depths near the SAFOD site.

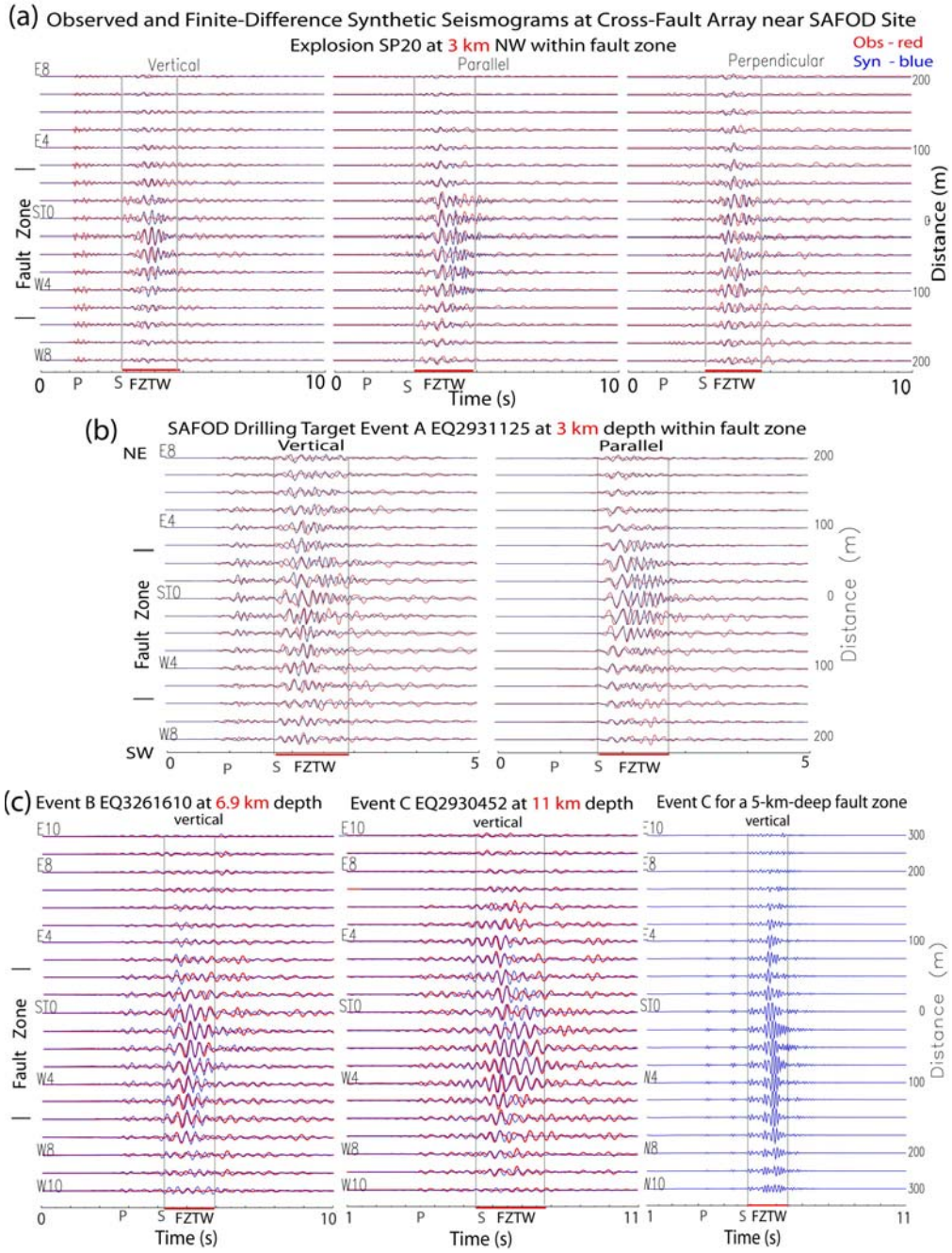

Fig. 15 Observed and 3-D finite-difference synthetic seismograms at the surface array across the SAF for **(a)** shot SP20, **(b)** the SAFOD drilling target event at ~3 km depth and 2 deep microearthquakes at depths of 7 km and 11 km (events B and C in Fig. 1 and Fig. 3a) using the velocity model in Fig. 11a. The fault zone extends to 12-km depth. An explosion source is used for shot and a double-couple source is used for earthquakes located within the fault zone at the focal depths. Seismograms have been <8 Hz filtered and are plotted using a fixed amplitude scale for all traces in each profile. **(c)** In contrast, the computed seismograms using a shallow fault zone truncated at 5-km depth for event C show much shorter wavetrains of FZTWs than those in recorded seismograms for this earthquake.

The coincidence of low seismic velocity [e.g. *Thurber et al.*, 2006; Li et al., 2004], high conductivity and Poisson's ratio [*Unsworth et al.,* 1997] suggests that a zone of fluid saturated breccia on the San Andreas fault at Parkfield may extend to the depth of at least ~7-8 km. We interpret that the distinct low-velocity core zone was formed by repeated damage during recurrent *M*6 earthquakes and other large events on the principal slip plane at Parkfield. The width of the low-velocity waveguide inferred by trapped waves likely represents the macroscopic damage extent in dynamic rupture and microscopic fault process zone accumulating mechanical, chemical, thermal, and other kinematical processes. The variation in velocity reduction along the fault zone and with depth may be caused by changes in overburden pressure, rock type, stress and slip rate, fault geometry, fluid content, and dynamic rupture during past earthquakes.

The damage zone at seismogenic depths may be caused by intense fracturing during earthquakes, including brecciation. Alternatively, given the fluid leakages currently taking place into the SAFOD well, the cause might relate to liquid-saturation and high pore-fluid pressure nears the fault. However, pore fluids arising from depth appear to hold a complex relationship with this damage zone, with its outer portions appearing to be more permeable than its core [*Lockner et al.*, 2000]. Moreover, the damage zone may actually form more of a fluid barrier which fluids are simply pounded against. The damage zone is also asymmetric, apparently broader on the southwest side of the main fault trace. The asymmetry may imply that the fault has a moving damage zone or that when it ruptures it may preferentially damage the already weakened rocks [*Chester et al.*, 1993]. Alternately, greater damage may be inflicted in the extensional quadrant than the compressional quadrant near the propagating crack tip [*Andrews*, 2005]. Although the structural model shown in Fig. 11a accounts for the FZTWs observations and its parameters at ~3 km depth are confirmed by the measurements directly in the SAFOD main-hole, it is likely to represent a gross average of the actual fault-zone structure at Parkfield. The true structure in 3-D will certainly be more complicated, and the damage magnitude and extent will vary along the fault strike and depth due to rupture distributions and stress variations over multiple length and time scales.

References

Andrews, D. J. (2005), Rupture dynamics with energy loss outside the slip zone, *J. Geophys. Res., 110*, B01307, dio: 0.1029.

Chester, F. M., J. P. Evans, and R. L. Biegel, Internal structure and weakening mechanisms of the San Andreas fault, *J. Geophys. Res*., *98*, 771-786, 1993.

Ellsworth, W. L., and P. E. Malin (2006), A first observation of fault guided PSV-waves at SAFOD and its implications for fault characteristics, *EOS, Transactions, and American Geophysics Union*, *87*, T23E-02, p154.

Graves, R. W., Simulating seismic wave propagation in 3D elastic media using staggered-grid finite differences, *Bull. Seismol. Soc. Am., 86*, 1091-1106, 1996.

Hickman, S. H., M. D. Zoback, and W. L. Ellsworth, Structure and Composition of the San Andreas fault zone at Parkfield: Initial results from SAFOD Phase 1 and 2, *EOS, Transactions, and American Geophysics Union*, *83*, No.47, p237, 2005.

Li，Y. G.，J. E.，Vidale，and S. E. Cochran，Low-velocity damaged structure of the San Andreas fault at Parkfield from fault-zone trapped waves，*Geophy. Res. Lett.，31*， L12S06，2004.

Li ，Y. G ，and P. E. Malin, San Andreas Fault damage at SAFOD viewed with fault-guided waves, Geophys. Res. Lett., 35, L08304, doi:10.1029/2007GL032924 ， 2008.

Lin, G., Y.H. Wang, F. Guo, Y. J. Wang, and W. M. Fan, Geodynamic modelling of crustal deformation of the North China block: a preliminary study, J. Geophys. And Eng., 1 63, DOI: 10.1088/1742-2132/1/1/008, 2004.

Lockner, D., H. Naka, H. Tanaka, H. Ito, and R. Ikeda (2000), Permeability and strength of core samples from the Nojima fault of the 1995 Kobe earthquake, *USGS Open file, Report* 00-129, 147-152.

Malin, P. M., E. Shalev, H. Balven, and C. Lewis-Kenedi (2006), Structure of the San Andreas Fault at SAFOD from P-wave tomography and fault-guided wave mapping,, *Geophys. Res. Letter 33*, No. 13, pp. 13314, 2006GL025973.

Thurber, C., S. Roecker, H. Zhang, S. Baher and W. Ellsworth, Fine-scale structure of the San Andreas fault zone and location of the SAFOD target earthquakes, Geophys. Res. Letter, 31, L12S02, doi:10.1029/2003GL019398, 2004.

Thurber, C., H. Zhang, F. Waldhauser, J. Hardebeck, A. Michael and D. Eberhart-Phillips , Three-dimensional compressional wavespeed model, earthquake relocations, and focal mechanisms for the Parkfield, California, region, Bull. *Seism. Soc. Am.* v. 96, no. 4B; p. S38-S49; DOI: 10.1785/0120050825, 2006.

Unsworth, M., P. Malin, G. Egbert, and J. Booker, Internal structure of the San Andreas fault at Parkfield, CA, *Geology*, 356-362, 1997.

Appendix III. Full-3D waveform tomography for fault-zone seismic structure

Tomographic inversions based solely on fault-zone guided waves are constrained by the specific source-receiver geometries, source mechanisms and fault-zone properties that can effectively generate these waves with sufficient signal-to-noise ratio. These constraints limit the amounts and the types of seismic data that can be used in the inversions and the resolution of the imaging results. A better image of the fault zone is likely to be obtained by incorporating waveform data from different types of seismic phases in a unified inversion.

We start testing jointly inversion for 3D seismic velocity and attenuation structures within and around the San Andreas Fault Zone at the Parkfield area. Here, we address our problems by applying a full-3D waveform analysis and inversion method to simultaneously infer 3D seismic velocity (Vp and Vs) and attenuation quality factors (Qκ and Qμ). Specifically, we will analyze waveform data from a variety of seismic phases, including *P* and *S* waves, fault-zone guided waves, fault-zone head waves and fault-zone reflected waves, and measure frequency-dependent amplitude and phase residuals with respect to synthetic seismograms calculated from a 3D reference fault-zone model using the Generalized Seismological Data Functionals (GSDF) method (Gee & Jordan 1992). The GSDF phase and amplitude measurements are inverted for 3D perturbations to the reference model using 3D sensitivity (Fréchet) kernels that fully account for the effects of structure on amplitude and phase behavior of the seismic waveforms. The inverted model perturbations will be applied to the reference model and the whole procedure will be iterated until the misfit between observed and synthetic waveforms, as quantified using the frequency-dependent GSDF phase and amplitude measurements, is below a prescribed level.

We have formulated our time-lapse tomography in the framework of seismic interferometry (Lauterborn *et al.* 2003; Snieder 2006). The principle of interferometry is widely used in optics and now also finds applications in geophysical monitoring. Seismic coda wave interferometry has been used to monitor magma migration under volcanoes (Ratdomopurbo & Poupinet 1995, Grêt *et al.* 2005; Pandolfi *et al*. 2006; Wegler *et al.* 2006) and temporal variations in seismic velocity structures associated with fault zones (Poupinet *et al.* 1984; Nishimura *et al.* 2000, 2005). In our study, we will incorporate similar principles into our F3DT to characterize fault-zone material properties.

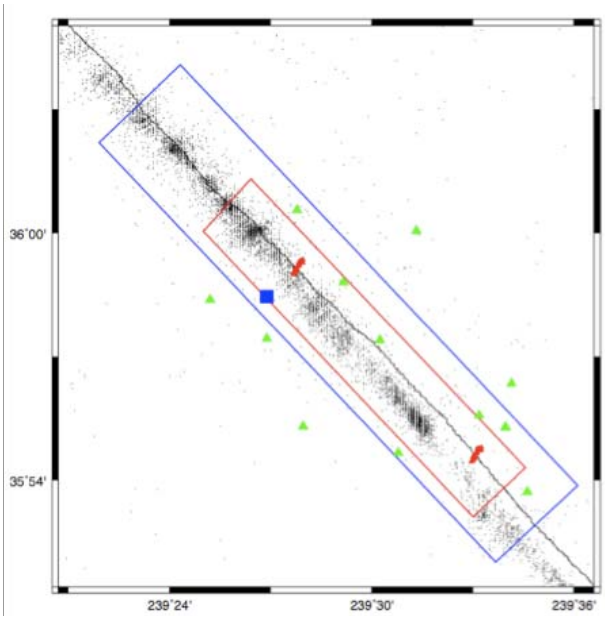

Figure 1. The San Andreas Fault Zone around the Parkfield area. Black solid line: San Andreas Fault main surface trace; blue square: SAFOD drilling site;
red bars: our dense surface array deployed near SAFOD in fall 2003 and near the town of Parkfield in 2002 and 2004; green triangles: HRSN borehole stations; black points: epicenters for earthquakes from 1965 to 2005 relocated by Thurber *et al.* (2006). Blue box shows our tomography target area with 50-meter grid-spacing; red box shows our high-resolution tomography area with 20-meter grid spacing.

The target area of our proposed tomographic study is shown in Figure 1. We will focus on imaging 3D fault-zone structure within a volume that is about 25-km-long along the fault strike, 12-km with depth and 5-km across fault. In our proposed tomographic inversion, we will include waveform data from the pilot-hole 3C geophones except for the data recorded at surface stations shown in Figure 1.

Methodology

The methodology that we will employ in our proposed study is the full-3D waveform tomography (F3DT) technique based on the scattering-integral formulation (Zhao *et al.* 2005; Chen *et al.* 2007a). Compared with classical ray-theoretic travel-time tomography, F3DT eliminates the highfrequency approximation and utilizes full waveform data instead of a single attribute of the data such as travel-time or amplitude. Moreover, F3DT can account for the nonlinearity of the structural inverse problem through iteration. For a given waveform dataset, F3DT will potentially provide the best resolution and accuracy. In full-wave tomography, the sensitivity (Fréchet) kernels are constructed from the exact solutions to the wave equation. It eliminates the high-frequency and structural-averaging approximations and accounts for all possible wave effects including diffraction, non-geometrical propagation and multipathing. The full-wave approach provides a practical and unified means for utilizing all seismic signals that are often discarded in conventional seismic tomography practice due to mathematical approximations.

We name those full-wave tomography techniques that derive 3D perturbations from 3D starting models full-3D tomography (F3DT). Currently, two types of F3DT techniques are being actively developed. One is based on minimizing an objective function defined in terms of waveform misfit using gradient-basedoptimization algorithms such as the conjugate-gradient method. The gradients of the objective function with respect to model parameters (elastic modulus, density, attenuation, etc.) are computed through adjoint wave propagation calculations. This type of method was first introduced to seismic exploration community in 1980s under the name "adjoint wavefield (state) method" (AWM) (Tarantola 1988) or "reverse-time migration" (McMechan 1983) and is currently being adapted for F3DT using natural earthquakes (Tromp *et al,* 2005; Liu & Tromp, 2006). The other methodology named "scattering-integral" (SI) method (Zhao *et al*. 2005; Chen *et al.* 2007ab) is based on explicitly constructing the Hessian of the objective function and minimizing the objective function using the Gauss-Newton method. The SI and AWM methods are closely related and they are based on exactly the same physical principles (Chen *et al*. 2007a). Compared with AWM, the SI implementation has two major advantages: first, the SI method can substantially reduce the amount of computing time for reaching convergence (Chen *et al*. 2007a); second, the SI method provides the capability for realtime source parameter inversion in a 3D Earth structure model (Zhao *et al.* 2006). The disadvantage of the SI method is that it requires a large amount of disk storage, but the storage cost can be significantly reduced by implementing efficient data compression algorithms (Wang & Wu 2000).

In our F3DT procedure, the RGTs are computed using purely numerical procedures such as FDM, FEM or SEM, therefore realistic 3D reference Earth structure models can be employed in the calculation and 3D wave propagation effects can be completely accounted for. A receiver Green tensor (RGT) Gik ($\mathbf{x}$, $t-\tau;\mathbf{x}_r$) for station r consists of the spatial-temporal wavefields generated by three orthogonal unit impulsive pointforces acting at the receiver location $\mathbf{x}_r$. The RGTs play a central role in our unified full-3D tomography and source parameter inversion algorithm. First, the RGTs are used for computing synthetic seismograms for arbitrary seismic sources in a 3D Earth structural model by applying the reciprocity principle; second, the RGTs are used for constructing full-wave Fréchet kernels using the scattering-integral formulation; third, the RGTs are exact Fréchet kernels of the waveforms with respect to the seismic moment tensor as a function of space and time, they therefore can be used for rapid seismic source parameter inversions in realistic 3D Earth structure models. In our proposed study, we will compute the RGTs for all stations in our modeling volume using the finite-difference method (FDM) (Olsen 1994; Graves 1996). We will construct a 3D reference (starting) model for the San Andreas Fault Zone at Parkfield using models from previous ray travel-time tomography (Thurber *et al.* 2004) and well-log data (Hickman *et al.* 2005). Before we use our 3D reference model for computing all the RGTs, we will validate our reference model by quantifying the misfit between observed and model predicted waveforms using frequency-dependent GSDF phase and amplitude residual measurements and make adjustments to the reference model if needed. Once RGTs for all stations in tomography area are constructed and stored, synthetic seismograms due to an arbitrary source located within our modeling volume can be constructed by applying the reciprocity principle. Storing all the RGTs will also provide us the capability to rapidly invert for seismic source parameters. The transposed RGT is the exact Fréchet kernel of the seismic waveform with respect to the stress glut and efficient algorithms can be developed to invert observed waveform data for source parameters based on the RGT database.

We quantify waveform misfit using a model based signal processing technique named Generalized Seismological Data Functionals or GSDF (Gee and Jordan, 1992). The frequency-dependent GSDF measurements are generalizations of the classic travel-time and t^* measurements to capture the waveform differences in frequency domain. To estimate the phase-delay time and amplitude-reduction time as functions of frequency, we developed the GSDF data analysis procedure. An example of GSDF data analysis is shown in Figure 2. To make the GSDF measurements, we first window the complete synthetic seismogram to isolate the wave group we want to model. The isolated wave group is termed "isolation filter" (Figure 2b). The isolation filter can contain any types of phases or just an arbitrary segment of the complete synthetic seismogram. The isolation filter is then cross-correlated with both the observed seismogram and the complete synthetic seismogram (Figure 2c and d). The resulting cross-correlagrams are then windowed around zero-lag and narrow-band filtered at a set of frequencies of interest. After the narrow-band filtering operation, the resulting cross-correlagrams can be well parameterized using a five-parameter Gaussian wavelet. The amplitude and phase differences between the data and the synthetic wavelets provide us the frequency-dependent GSDF measurements $\delta t\mathrm{p}(\omega n)$ and $\delta t\mathrm{q}(\omega n)$ at each narrow-band filtering frequency ωn (Figure 2e and f). The GSDF measurements of $\delta t\mathrm{x}(\omega n)$ (x = p, q) are weighted averages of $\delta\tau\mathrm{x}$ over narrow frequency-bands centered on the narrow-band filtering frequency ωn (Chen *et al.* 2007b). The effect of the averaging introduced by our measurement procedure is completely accounted for in our full-wave sensitivity kernels.

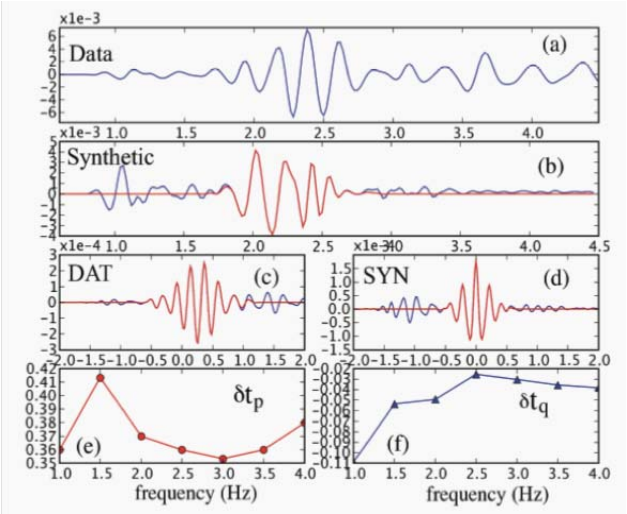

Figure 2. An example of GSDF analysis (a) Observed seismogram; (b) synthetic seismogram, the isolation filter is shown in red; (c) crosscorrelagram between the isolation filter and observed seismogram; (d) cross-correlagram between the isolation filter and the complete synthetic seismogram; (e) GSDF phase-delay time measurements made at 7 frequencies evenly distribution across 1-4 Hz frequency band; (f) GSDF amplitude-reduction time measurements. propagation, the resulting tomography model will not lose resolution due to mis-identification of certain phases.

The 3D sensitivity (Fréchet) kernels for our GSDF measurements with respect to seismic velocity and attenuation are computed using the "full-wave approach", (Zhao *et al.*, 2005; Chen *et al.* 2007a). First, we linearize the relation between GSDF measurements and waveform perturbation kernel accounting for the effect of all the measurement operations applied on the seismograms in order to obtain the data functionals such as convolving with the instrument response, cross-correlation, windowing and narrow-band filtering. Exact expressions of the seismogram perturbation kernel for GSDF measurements are given in Chen (2005). Second, we linearize the relation between waveform perturbation and the perturbation to the density and elastic/anelastic modulus tensor using the Born approximation. The exact Fréchet kernels for GSDF measurements with respect to density and elastic modulus can therefore be expressed as a function of the convolution between gradient of the forward earthquake wavefields with the gradient of the transposed receiver Green tensor (RGT) $Gik\ (\mathbf{x},\ t-\tau;\mathbf{x}_r)$. Similar equations for *P* and *S* velocity can be found in Zhao *et al.* (2005) or Chen *et al.* (2007b).

An example of the sensitivity kernels of frequency-dependent GSDF phase-delay measurements with respect to *S* velocity for a fault-zone-related seismic phase is shown in Figure 3. The fault zone model consists of a single 400m-wide (from -200m to 200m) homogeneous layer of low velocity zone sandwiched between two quarter-spaces. Fault-zone-parallel synthetic seismograms are shown for a double-couple source buried at 6 km depth in the middle of the low-velocity zone and recorded at 15 stations located at 15 km epicenter-distance and evenly

distributed across the low-velocity zone with 50m inter-station distances. We've computed the Fréchet kernels of frequency-dependent phase-delay time with respect to *S*-velocity for a large-amplitude wave on the center seismic trace. The shape of the kernels suggests that this wave primarily propagates within the low-velocity zone. The concentration of the sensitivity within the low-velocity zone increases with frequency. We note that different from the "banana-doughnut" kernels for direct arriving body-wave phases, for this particular phase, the sensitivity is nonzero on the ray path. The distribution of the sensitivity suggests that this phase is similar to the Love wave propagating in a horizontal low-velocity layer. Because both the forward earthquake wavefields and the RGTs were computed numerically using FDM, the Fréchet kernels constructed this way can account for the full physics of 3-D wave propagation.

The GSDF measurements of phase-delay and amplitude anomalies are inverted jointly for both seismic velocity and attenuation perturbations to the reference 3D Earth structure model. The resulting linear system is scaled using a data-weighting matrix which is a linear combination of the Laplacian operator (Constable *et al*., 1987; Sambridge, 1990; Tarantola, 2005) and the identity operator. Using this definition of the "roughing operator", we impose our prior information on the inversion; i.e., we assume that in the absence of any other information, the model perturbation is smooth and small. We note that the corresponding "smoothing operator" can be generated from an exponential correlation function, whose correlation length is proportional to λ. In practice, the Laplacian operator is approximated numerically by finite differencing. The final linear system that we solve contains the sensitivity kernels for each GSDF measurement. The linear system is solved using a parallelized LSQR subroutine from the PETSc parallel scientific computing library (Balay *et al.*, 2004). The LSQR method (Paige and Saunders, 1982), which is a type of conjugate-gradient method, provides a very efficient means for solving large-scale sparse linear systems. The model perturbation can be applied to the reference structure model, RGTs and synthetics as well as all the sensitivity kernels can be re-calculated using the updated structure model and the tomography procedure can be iterated a number of times to further improve and refine our seismic structure and/or source models. As shown in Chen *et al.* (2007a), this iterative procedure is equivalent to a Gauss-Newton optimization algorithm for minimizing a least-square summation of all the GSDF misfit measurements with a prescribed model regularization given by the model covariance matrix.

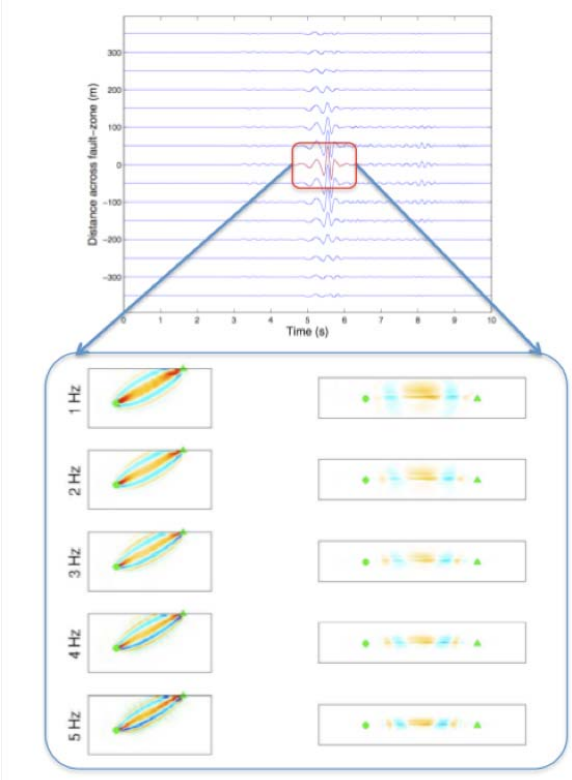

Figure 3. Upper panel shows synthetic seismograms computed for a simple 1D fault-zone model using FDM. Lower panel shows the crosssection (left column) and mapview (righ column) of the *S*-velocity kernels for phase-delay times on the seismic waveform within the red box at frequencies ranging from 1Hz to 5Hz. The color schemes are such that white represents zero; warm colors (yellow to orange to red) represent negative amplitudes indicating that a velocity increase leads to an advance in arrival time; and cool colors (light to dark blue) represent positive amplitudes indicating a velocity increase leads to a delay in arrival time. Green dots and triangles show source and station locations. The cross-section is at the source-receiver
plane; the mapview is at 3km depth. The sensitivity is largely concentrated within the low-velocity zone. Sensitivity to structures outside the low-velocity zone increases at lower frequencies. The asymmetry of the kernel in the mapviews is caused by source mechanism.

In the next step, we will collect and compile a seismogram dataset for our F3DT inversion and constructing a reference structural model by combining existing models for our target area and by forward waveform modeling for a subset of seismograms. The quality of our 3D reference model will be assessed by quantifying waveform differences between observed and synthetic waveforms for a subset of our dataset using the GSDF method. Since the GSDF measurements are only weakly nonlinear with respect to structure model, by examining the GSDF misfit measurements we can manually adjust our reference model accordingly. We note that one important advantage of our F3DT methodology is that we do not require the reference model to be very close to the true model, which is a consequence of using the Rytov approximation for waveform linearization (Chen *et al.* 2007ab).

Then, we will carry out F3DT for two iterations, the first iteration in the bigger box in Figure 1 with 50-meter grid-spacing and the second iteration in the smaller box with 20-meter grid-spacing and using the result from the first iteration as the reference model. For each iteration, we will complete (1) computing RGTs, (2) inverting for source parameters and making GSDF measurements, (3) constructing sensitivity kernels, (4) inverting for model perturbations.

References

Chen, P., Z. Li and T. Jordan, Full 3D tomography for crustal structure of the Los Angeles region, , Bull. Seism. Soc. Am., Vol. 97, No. 4, pp. 1094-1120, doi: 10.1785/0120060222, 2007a.

Chen, P., Z. Li and T. Jordan, Full 3D waveform tomography: A comparison between the scattering-integral and adjoint-wavefield methods. Geophys. J. Int., DOI: 10.1111/j.1365-246X.2007.03429. 2007b.

Constable, S. C., R. L. Parker, and C. G. Constable. Occam's inversion: a practical algorithm for generating smooth models from electromagnetic sounding data, *Geophysics* **52,** 289–300, 1987.

Gee, L. S., and T. H. Jordan, Generalized seismological data functionals, *Geophys. J. Int.* **111,** 363–390, 1992.

Graves, R. W., Simulating seismic wave propagation in 3D elastic media using staggered-grid finite differences, *Bull. Seismol. Soc. Am., 86*, 1091-1106, 1996.

Li, Y.-G. and P. Chen, Full-3D Waveform Tomography for the Seismic Velocity and Attenuation Structure on the San Andreas Fault Zone in Parkfield Area, *Eos Trans. AGU, 89*(53), Fall Meet. Suppl. 2008.

Paige, C. C., and M. A. Saunders (1982). LSQR: sparse linear equations and least squares problems, *ACM Trans. Math. Software* **8,** 195–209.

Sambridge, M. S., Non-linear arrival time inversion: constraining velocity anomalies by seeking smooth models in 3-D, *Geophys. J. Int.* 102, 653–677, 1990.

Tarantola, A. , *Inverse Problem Theory and Methods for Model ParameterEstimation*, Society for Industrial and Applied Mathematics, Philadelphia, Pennsylvania, 342 pp, 2005.

Thurber, C., H. Zhang, F. Waldhauser, J. Hardebeck, A. Michael and D. Eberhart-Phillips , Three-dimensional compressional wavespeed model, earthquake relocations, and focal mechanisms for the Parkfield, California, region, Bull. *Seism. Soc. Am.* v. 96, no. 4B; p. S38-S49; DOI: 10.1785/0120050825, 2006.

Zhao, L., T. H. Jordan, K. B. Olsen, and P. Chen, Fre´chet kernels for imaging regional Earth structure based on three-dimensional reference models. *Bull. Seism. Soc. Am.* **95,** no. 6, 2066–2080, 2005.

Appendix IV. Understanding fault zone compliance: Seismic probing of InSar anomalies

Coseismic interferograms for both the Landers and Hector Mine earthquakes showed strain localized on the Calico fault as well as other nearby faults. Line of sight (LOS) displacements with amplitudes of a few centimeters and wavelengths of a few kilometers are clearly associated with the Calico fault trace. The InSAR observations are best explained with a 1–2 km wide zone around the fault with a shear modulus reduced by 50% and extending to at least 5 km depth [*Fialko et al.*, 2002].

We conducted a detailed seismic investigation of the Calico fault to: (i) test the interpretation of the anomalous strain detected by InSAR as elastic deformation of compliant zones in response to coseismic loading, and (ii) determine if the variations in static moduli observed with InSAR are similar to dynamic moduli variations observed with seismic data. We installed a dense array of 40 intermediate period stations and 60 short-period stations in a 1.5 km by 5.5 km grid adjacent to the Calico fault. We detonated three shots and recorded background seismicity for 6 months. We applied three independent methods to determine the fault structure of the Calico fault: 1) finite-difference modeling of fault-zone trapped waves, 2) travel-time modeling of P arrival times, and 3) static stress modeling of the compliant zone in response to the Landers and Hector Mine earthquakes.

Seismic and geodetic data from the Calico fault reveal a wide zone of reduced seismic velocities and effective elastic moduli. Using seismic travel times, trapped waves, and interferometric Synthetic Aperture Radar observations, we document seismic velocities reduced by 40 - 50% and shear moduli reduced by 65% compared to wall-rock in a 1.5-km-wide zone along the Calico fault. Observed velocity reductions likely represent the cumulative mechanical damage from past earthquake ruptures. No large earthquake has broken the Calico fault in historic time, implying that fault damage persists for hundreds or perhaps thousands of years. These findings indicate that faults can affect rock properties at substantial distances from primary fault slip surfaces, and throughout much of the seismogenic zone, a result with implications for the portion of energy expended during rupture to drive cracking and yielding of rock and development of fault systems. A wide, persistent compliant zone along a fault identifies a region that is most likely weaker than the surrounding rock, facilitating the localization of regional strain. Strain localization leads to faults that are more responsive to relatively small stress changes; thus enhancing the tendency for earthquakes to rupture well-established faults rather than more intact rock. Permanent damage zones may thus play a critical role in the development and dynamics of faults, fault systems, and thus plate boundaries.

We have established a data-base of this research project via IRIS/PASSCAL software (Antelope) and put the field data, station information and first-arrival times for part of a couple hundreds of earthquakes and 3 explosions in this database.

Paper and Conference Abstracts:

Cochran, E. S., Y. G Li, P. M. Shearer, S. Barbot, Y. Fialko, and J. E. Vidale, Seismic and geodetic evidence for extensive, long-lived fault damage zones, Geology, in press, 2008.

Cochran, E. S., Y. G. Li, P. M. Shearer, J. E. Vidale, and Y. Fialko, Calico Fault Structure Determined Using Traveltime Data from Seismicity and Explosions, AGU Fall Meeting, 2007.

Cochran, E. S., M. Radiguet, P. M. Shearer, Y.-G. Li, Y. Fialko, and J.E. Vidale, Seismic imaging of the damage zone around the Calico fault, AGU Fall Meeting, 2006.

Seismic and Geodetic Evidence For Extensive, Long-Lived Fault Damage Zones

Elizabeth S. Cochran[1], Yong-Gang Li[2], Peter M. Shearer[3], Sylvain Barbot[3], Yuri Fialko[3], and John E. Vidale[4]

ABSTRACT

During earthquakes slip is often localized on preexisting faults, but it is not well understood how the structure of crustal faults may contribute to slip localization and energetics. Growing evidence suggests that the crust along active faults suffers anomalous strain and damage during large quakes (*Fialko et al.*, 2002; *Vidale and Li*, 2003; *Li et al.*, 1998; *Ben-Zion et al.*, 2003; *Li et al.*, 2006; *Mamada et al.*, 2004; *McGuire and Ben-Zion*, 2005). Seismic and geodetic data from the Calico fault in the eastern California shear zone reveal a wide zone of reduced seismic velocities and effective elastic moduli. Using seismic travel times, trapped waves, and interferometric Synthetic Aperture Radar observations, we document seismic velocities reduced by 40 - 50% and shear moduli reduced by 65% compared to wallrock in a 1.5-km-wide zone along the Calico fault. Observed velocity reductions likely represent the cumulative mechanical damage from past earthquake ruptures. No large earthquake has broken the Calico fault in historic time, implying that fault damage persists for hundreds or perhaps thousands of years. These findings indicate that faults can affect rock properties at substantial distances from primary fault slip surfaces, and throughout much of the seismogenic zone, a result with implications for the portion of energy expended during rupture to drive cracking and yielding of rock and development of fault systems.

INTRODUCTION

Previous seismic studies have suggested that fault damage zones are only a few hundred meters wide. Studies along the 1992 M_w7.3 Landers earthquake, the 1999 M_w7.1 Hector Mine earthquake, and the 1999 M_w7.4 Izmit earthquake characterized the fault damage region as a zone 100 – 200 m wide with seismic velocity reductions of 20 – 40 percent (*Vidale and Li*, 2003; *Li et al.*, 1998; *Ben-Zion et al.*, 2003). A study of the 2004 M_w6.0 Parkfield earthquake showed shear wave velocities in a 200 m wide damage zone were further reduced 1.0 – 1.5%, with recovery of seismic velocities observable in subsequent months (*Li et al.*, 2006). Fault damage zone healing has also been reported in the years to decades following a mainshock (*Vidale and Li*, 2003; *Li et al.*, 1998). However, it is not currently known if fault zone damage persists over a full earthquake cycle, which may last hundreds to thousands of years. Thus, understanding the fault zone structure and degree of damage along a major crustal fault has implications for localization of strain, triggering of earthquakes, and the mechanics of earthquake rupture. Here we combine seismic and geodetic data from the Calico fault, which has remained unbroken in historical times, to probe the structure and long-term properties of fault damage zones.

The Calico fault is located within the eastern California shear zone (ECSZ), midway between the 1992 M_w7.3 Landers and 1999 M_w7.1 Hector Mine ruptures (Fig. 1A). The NW striking Calico fault has accumulated ~10 km of dextral slip since its inception (*Dokka and Travis*, 1990; *Oskin et al.*, 2007). The Calico fault has the highest average dextral slip rate within the ECSZ, roughly 1–2 mm/yr (*Dokka and Travis*, 1990; *Oskin et al.*, 2007), and some geodetic estimates suggest much higher slip rates up to 7 mm/yr (*Peltzer et al.*, 2001). Earthquakes on the Mojave Desert portion of the ECSZ faults have extremely long recurrence times on the order of a few thousand years (*Rubin and Sieh, 1997*), but are inferred to cluster in time (*Rockwell et al.*, 2000). While paleoseismic studies on the Calico Fault are sparse, recent trench data indicate that the last earthquake occurred at least several hundred years ago (*Ganev et al.*, 2008).

Coseismic interferograms for both the Landers and Hector Mine earthquakes showed strain localized on the Calico fault as well as other nearby faults (*Fialko et al.*, 2002; *Fialko*, 2004). Line of sight (LOS) displacements with amplitudes of a few centimeters and wavelengths of a few kilometers are clearly associated with the Calico fault trace (Fig. 1B). Initial interpretation of the InSAR anomalies for the Calico fault suggested triggered slip (*Sandwell et al.*, 2000), but this required left-lateral movement opposite to the long-term motion. An alternative interpretation held that the InSAR observations are best explained with a 1–2 km wide zone around the fault with a shear modulus reduced by 50% extending to at least 5 km depth (*Fialko et al.*,

2002). These geodetic results suggest a fault zone width (~2 km) an order of magnitude greater than generally reported for low velocity zones on major faults determined using seismic data (200 m) (*Li et al.*, 1998; *Ben-Zion et al.*, 2003; *Li et al.*, 2006; *Mamada et al.*, 2004; *McGuire and Ben-Zion*, 2005).

DATA ANALYSIS

We conducted a detailed seismic investigation of the Calico fault to: (i) test the interpretation of the anomalous strain detected by InSAR as elastic deformation of compliant zones in response to coseismic loading, and (ii) determine if the variations in static moduli observed with InSAR are similar to dynamic moduli variations observed with seismic data. We installed a dense array of 40 intermediate period stations and 60 short-period stations in a 1.5 km by 5.5 km grid adjacent to the Calico fault (Fig. 1B). We detonated three shots and recorded background seismicity for 6 months. We applied three independent methods to determine the fault structure of the Calico fault: 1) finite-difference modeling of fault-zone trapped waves, 2) travel-time modeling of P arrival times, and 3) static stress modeling of the compliant zone in response to the Landers and Hector Mine earthquakes.

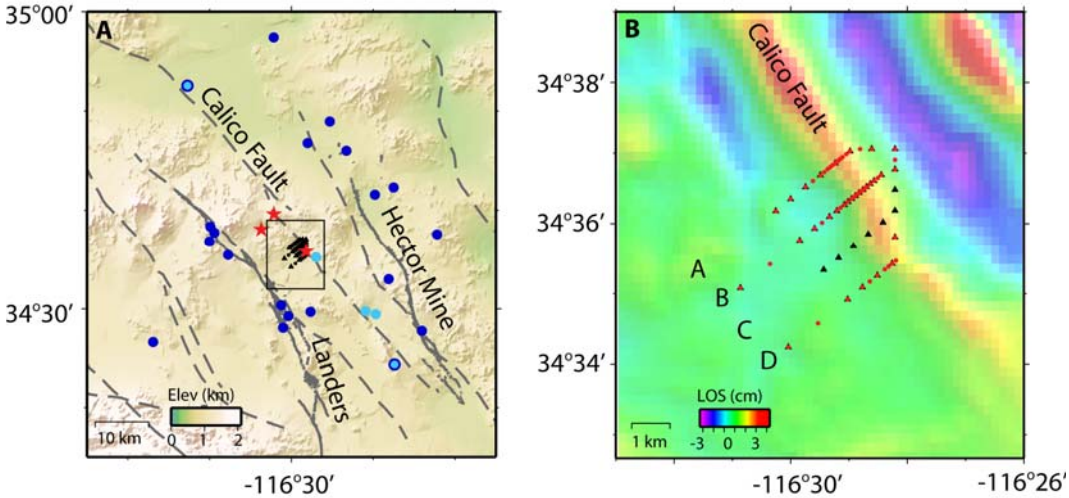

Figure 1. Overview map of station and event distribution. (A) A shaded relief map of the Mojave Desert region. Regional faults are shown by dashed gray lines and the Landers and Hector Mine ruptures are shown by solid gray lines. Light and dark blue circles indicate local earthquakes used in the fault zone trapped wave and travel-time analyses, respectively. Light blue circles with a dark blue outline were used in both analyses. Red stars denote shots. Black triangles and circles show seismic stations. The gray square outlines the region in Figure 1B. (B) High-pass-filtered coseismic interferogram from the 16 October 1999 Hector Mine earthquake that spans the time period from 13 January 1999–20 October 1999 (after *Fialko et al.,* 2002). Colors denote variations in the line of sight (LOS) displacements. Black triangles and red circles are intermediate-period and short-period seismic stations.

Fault-zone trapped waves are seismic waves confined within the low velocity structure adjacent to the fault that are excited by earthquakes or explosions located within the fault zone. Thus, the trapped wave analysis is limited to events that occurred on or relatively close to the Calico fault; here we present results derived from 2 shots and 5 local earthquakes (see Data Repository). Full synthetic waveforms are computed for each event-station pair using a 3D finite-difference scheme and compared to actual waveforms (Fig. 2). We vary the damage zone width, depth, and velocity reduction to determine the best fit to the data. The width of the zone is controlled mostly by the observation of high-amplitude trapped waves following the S arrival on stations near the fault trace. If the damage zone extends across the seismogenic zone, the envelope of the trapped wave will have a longer duration for deeper earthquakes. For the deepest on-fault earthquake, at a depth of 10.8 km, we see a clear increase in the duration of the trapped wave energy envelope.

Travel-time analysis allows us to map the seismic velocities across the grid of seismic stations. The velocity reduction within the Calico fault damage zone is substantial, as indicated by delays in the body wave arrivals near the fault (Fig. 3). We do not have sufficient ray coverage to perform a tomographic inversion for the 3-D velocity structure under our array; instead we determine the fault zone models that best fit the P arrivals from shots and earthquakes (Fig. 1). Events

chosen for this study were well recorded by the array, have good signal-to-noise ratios, and cover a range of back azimuths to best image the entire fault zone. We modeled 3 shots, 20 local earthquakes and 8 teleseismic earthquakes. We compute travel times based on the graph theory technique of *Moser* (1991), modified as described in *Nolet et al.* (2005), to get stable results for the strong 3-D velocity variations in our models.

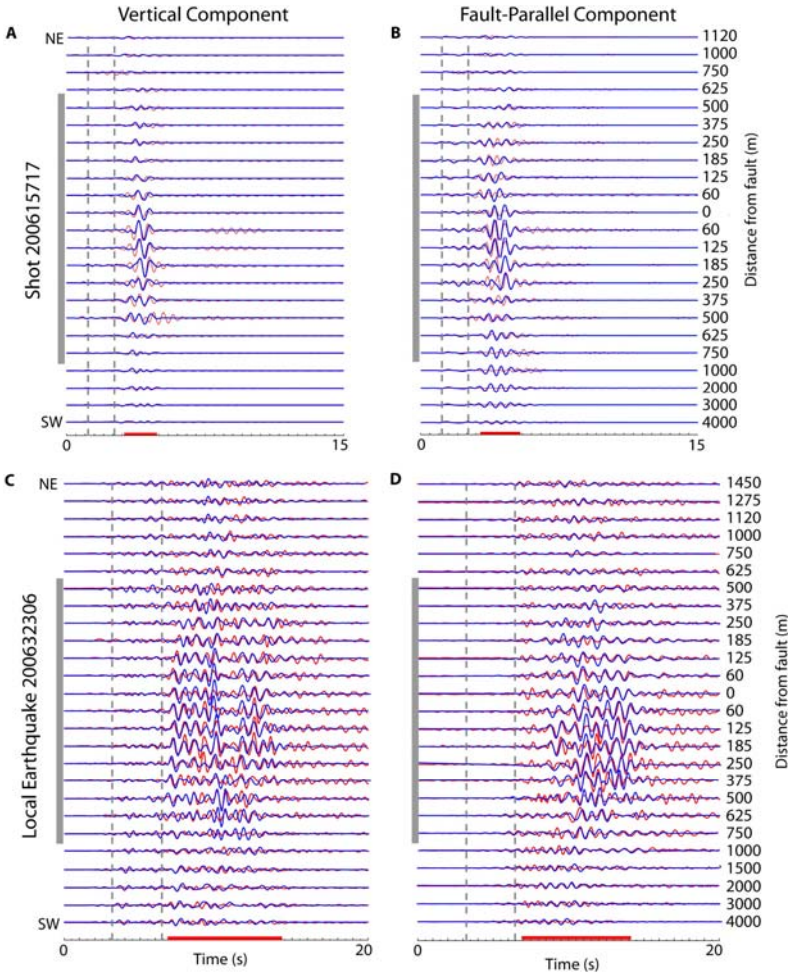

Figure 2. Recorded and synthetic fault zone trapped wave data. (A) Recorded (red) and synthetic (blue) vertical seismograms for shot 200615717. The vertical dashed lines indicate the P and S wave arrivals. The red bar indicates the approximate timing of strong trapped wave energy. The width of the compliant zone is shown by the vertical gray bar (~1.5 km wide). Synthetic seismograms were computed using the model shown in Figure 4 with an S velocity reduction of 50% as described in the text. (B) Recorded (red) and synthetic (blue) fault-parallel seismograms for shot 200615717. (C) Recorded (red) and synthetic (blue) vertical seismograms for local earthquake 200632306. (D) Recorded (red) and synthetic (blue) fault-parallel seismograms for local earthquake 200632306. Data are low-pass filtered at 2 Hz.

RESULTS

The best-fit fault models were initially determined independently for the fault zone trapped wave, travel-time, and InSAR data sets. The model results for the three data sets were surprisingly consistent, so we fit all of the data to a single model (see Data Repository) (Fig. 4A). We find that the fault zone is roughly 1.5 km wide with a P-wave velocity reduction of ~40%, with similar misfits seen in a range between 30%–50%. There is some tradeoff between the velocity reduction and the width of the fault; models with fault zone widths between 1 and 2 km fit the data with nearly the same misfit. The lateral velocity profile across the fault is approximated as a Hanning taper and the velocity reduction tapers linearly to zero between 0 and 12 km depth.

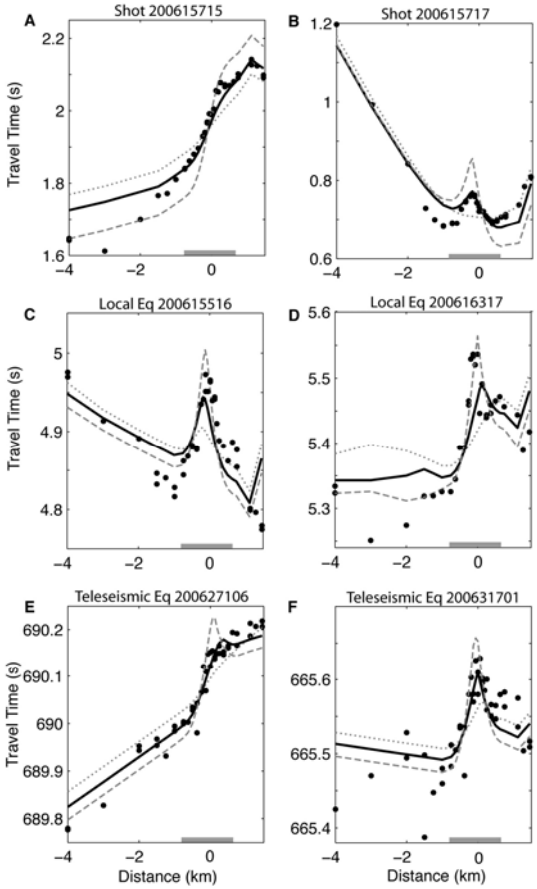

Figure 3. Travel time data and forward model comparison. Examples of the fits of several models with different velocity reductions (lines) to the travel time data (points) across Line B (see Fig. 1). Fault zone geometry is shown in Figure 4. Models shown are 10% velocity reduction (dotted gray line), 40% velocity reduction (solid black line), 70% velocity reduction (dashed gray line). The solid line denotes the preferred model as described in the text. Data are shown for events: (A) Shot 200615715 (B) Shot 200615717, (C) Local earthquake 200615516, (D) Local earthquake 200616317, (E) Teleseismic earthquake 200627106, and (F) Teleseismic earthquake 200631701. Grey bar represents the modeled 1.5 km width of the low velocity zone.

The damage zone is modeled to extend to 12 km depth, but with small relative velocity reductions below ~5 km (Fig. 4A). Synthetic waveforms are well fit to the fault zone trapped wave data (Fig. 2), showing a clear increase in trapped energy within 750 m of the fault trace. Modeled and actual travel-time plots show similar width and amplitude for the velocity anomaly along the Calico fault (Fig. 3). The depth of the zone is constrained by a single near-fault earthquake, located 27.9 km away and 10.8 km deep, with extended trapped wave energy that cannot be matched using a model with a shallow damage zone (see Data Repository).

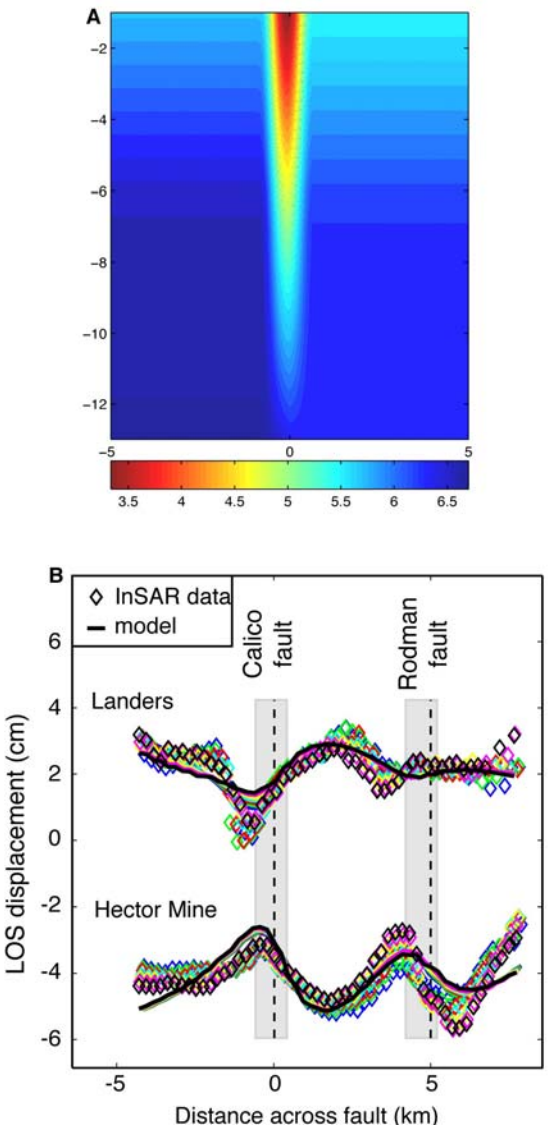

Figure 4. Best fit model and InSAR model and data. (A) Model of the P-wave low velocity zone along the Calico Fault with a 40% reduction in velocity. Additional parameters are described in the text. (B) Observed LOS displacements across the Calico Fault (color diamonds) and predictions for the best-fitting model using the geometry shown in Figure 4A, but with reduced by 65% and reduced by 30%. Color diamonds represent different swaths perpendicular to the Calico fault

To test whether the seismically imaged fault zone is consistent with available geodetic data, we modeled the response of the best-fitting compliant structure (Fig. 4) to static stress changes due to the Landers and Hector Mine earthquakes. We

converted the seismic velocity model (Fig. 4A) into elastic moduli assuming a constant density. The resulting 2-D variations in elastic moduli were extrapolated along the Calico fault to obtain a 3-D fault zone model. A similar compliant structure was also introduced around the nearby Rodman fault. We calculated the coseismic deformation due to the compliant zones using the equivalent body force method in the spectral domain (*Barbot et al.*, 2008). Figure 4B shows the observed displacements in the satellite line of sight (LOS) across the Calico fault and predictions for the best-fitting seismic tomography model. The modeled response of the Calico fault zone is in good agreement with InSAR data, indicating that the same variations in moduli between the fault zone and the ambient crust can account for both the static (geodetic) and dynamic (seismic) deformation. The InSAR data cannot be fit with a shallow compliant zone and thus provide an additional constraint on the fault zone depth. Both the InSAR and fault zone trapped waves indicate the damage zone likely extends to at least 5 km depth, but is narrower and with a lower velocity contrast at greater depths.

DISCUSSION

As documented here, we observe a 1.5 km wide zone with seismic wave velocities reduced up to 40%–50% and a shear modulus reduced by 65% along the Calico fault. This zone likely represents a region of mechanically weakened, or damaged, rocks related to the cumulative effect of past ruptures (Fig. 4B). The damage zone imaged along the Calico fault is much wider than those reported by previous seismic observations on neighboring faults, 1.5 km versus 200 m. This apparent discrepancy might result because most seismic studies of fault zones were initiated following a large mainshock (*Vidale and Li*, 2003; *Li et al.*, 1998, *Ben-Zion et al.*, 2003; *Li et al.*, 2006) rather than late in the interseismic period. These studies focused on narrow zones that may be more highly damaged immediately following a large earthquake, but heal subsequently. Perhaps most importantly, most previous studies did not deploy arrays at great enough distances from the fault to see the wide damage zone implied here. These studies may not have seen the true edge of the fault zone, but were comparing the highly damaged portion of the fault to the less damaged region 200-300 m from the main slip plane.

Some geologic and studies have also indicated that fault deformation zones can extend to greater distances from the main slip plane. Recently, an aftershock study concluded that the Landers rupture has a 300 m wide low velocity zone that extends to at least 7 km depth (*Li et al.*, 2007), where previous studies indicated only a 180 m wide zone (*Li et al.*, 1998). A wide (1–2 km) damage zone was inferred on the Calaveras fault from observations of fault zone trapped waves on a widely spaced array (*Spudich and Olsen*, 2001). *Oskin et al.* (2007) reported deflection of the Silver Bell fault by distributed shear adjacent to the Calico fault over a width comparable to the damage zone imaged here.

Differences in the inferred widths of compliant zones may also be due to intrinsic variations in the width of damaged zones around different faults, as well as along different sections of the same fault. Substantial changes in the effective width of the compliant zone of the Calico fault along strike are apparent in the InSAR line of sight (LOS) displacements. Observations using dense geodetic networks revealed several localized zones of high interseismic strain along the San Andreas fault that were attributed to compliant fault zones (*Lisowski et al.*, 1991; *Chen and Freymueller*, 2002). Detailed mapping of near-field interseismic deformation may provide further insights into the ubiquity and spatial variability of permanent damage around active faults.

Results presented in this study indicate that faults can affect rock properties at greater distances than generally documented. The observed reduction in the elastic rigidity of a wide zone surrounding the primary slip surface is likely a result of wallrock fracturing and yielding during earthquakes. Quantifying the degree and spatial extent of fault zone damage provides constraints on the portion of fracture energy expended during rupture (e.g. *Fialko*, 2007). A wide, persistent compliant zone along a fault identifies a region that is most likely weaker than the surrounding rock, facilitating the localization of regional strain. Strain localization leads to faults that are more responsive to relatively small stress changes; thus enhancing the tendency for earthquakes to rupture well-established faults rather than more intact rock. Permanent damage zones may thus play a critical role in the development and dynamics of faults, fault systems, and thus plate boundaries.

ACKNOWLEDGEMENTS

We thank all of the field volunteers for their hard work under the blazing Mojave sun. We thank Guust Nolet for providing ray tracing software. This research was supported by NSF (EAR-0439947) and SCEC (contribution number 1185).

REFERENCES CITED

Barbot, S., Fialko, Y., and Sandwell, D., 2008, Effect of a compliant fault zone on the inferred earthquake slip distribution, Journal of Geophysical Research, 113, B06404, doi:10.1029/2007JB005256, 2008.

Ben-Zion, Y., Peng, Z., Okaya, D., Seeber, L., Armbruster, J. G., Ozer, N., Michael, A. J., Baris, S., Aktar, M., 2003, A shallow fault-zone structure illuminated by trapped waves in the Karadere–Duzce branch of the North Anatolian Fault, western Turkey: Geophysical Journal International, v. 152, p. 699–717, doi: 10.1046/j.1365-246X.2003.01870.x.

Chen, Q., and Freymueller, J., 2002, Geodetic evidence for a near-fault compliant zone along the San Andreas fault in the San Francisco bay area: Bulletin of the Seismological Society of America, v. 92, p. 656–671, doi: 10.1785/0120010110.

Dokka, R.K., and Travis, C.J., 1990, Late Cenozoic strike-slip faulting in the Mojave Desert, California: Tectonics, v. 9, p. 311–340, doi: 10.1029/TC009i002p00311.

Fialko, Y., Sandwell, D., Agnew, D., Simons, M., Shearer, P., Minster, B., 2002, Deformation on nearby faults induced by the 1999 Hector Mine earthquake: Science, v. 297, p. 1858–1862, doi: 10.1126/science.1074671.

Fialko, Y., 2004, Probing the mechanical properties of seismically active crust with space geodesy: Study of the coseismic deformation due to the 1992 M w 7.3 Landers (southern California) earthquake: Journal of Geophysical Research, v. 109, p. B03307, doi: 10.1029/2003JB002756.

Fialko, Y., 2007, Fracture and frictional mechanics – Theory: Treatise on Geophysics, v. 4, p. 83–106.

Ganev, P.N., Dolan, J.F., Oskin, M.E., Owen, L.A., and Le, K.N., 2008, Paleoseismologic Evidence for Multiple Holocene Earthquakes on the Calico Fault: Implications for Earthquake Clustering in the Eastern California Shear Zone, Southern California Earthquake Center Annual Meeting Proceedings and Abstracts, Volume XVIII, p. 153-154.

Li, H., Zhu, L., and Yang, H., 2007, High-resolution structures of the Landers fault zone inferred from aftershock waveform data: Geophysical Journal International, v. 171, p. 1295–1307.

Li, Y.-G., Chen, P., Cochran, E.S., Vidale, J.E., and Burdette, T., 2006, Seismic evidence for rock damage and healing on the San Andreas Fault associated with the 2004 M 6.0 Parkfield earthquake: Bulletin of the Seismological Society of America, v. 96, p. S349–S363, doi: 10.1785/0120050803.

Li, Y.-G., Vidale, J.E., Aki, K., Xu, F., and Burdette, T., 1998, Evidence of shallow fault zone strengthening after the 1992 M7.5 Landers, California, earthquake: Science, v. 279, p. 217–219, doi: 10.1126/science.279.5348.217.

Lisowski, M., Savage, J.C., and Prescott, W.H., 1991, The velocity field along the San Andreas fault in central and southern California: Journal of Geophysical Research, v. 96, p. 8369–8389, doi: 10.1029/91JB00199.

Mamada, Y., Kuwahara, Y., Ito, H., and Takenaka, H., 2004, Discontinuity of the Mozumi–Sukenobu fault low-velocity zone, central Japan, inferred from 3-D finite-difference simulation of fault zone waves excited by explosive sources: Tectonophys. v. 378, p. 209–222, doi: 10.1016/j.tecto.2003.09.008.

McGuire, J., and Ben-Zion, Y., 2005, High-resolution imaging of the Bear Valley section of the San Andreas fault at seismogenic depths with fault-zone head waves and relocated seismicity: Geophysical Journal International, v. 163, p. 152–164, doi: 10.1111/j.1365-246X.2005.02703.x.

Moser, T.J., 1991, Shortest path calculation of seismic rays: Geophys. v. 56, p. 59–67, doi: 10.1190/1.1442958.

Nolet, G., Dahlen, F.A., and Montelli, R., Traveltimes and amplitudes of seismic waves: a re-assessment. *Array analysis of broadband seismograms: Geophys. Monograph Ser. (eds. A. Levander & G. Nolet)*. **157**, 37–48 (2005).

Oskin, M., Peng, L., Blumentritt, D., Mukhopadhyay, S., and Iriondo, A., 2007, Slip rate of the Calico fault: Implications for geologic versus geodetic rate discrepancy in the eastern California shear zone: Journal of Geophysical Research, v. 112, p. B03402, doi: 10.1029/2006JB004451.

Peltzer, G., Crampe, F., Hensley, S., and Rosen, P., 2001, Transient strain accumulation and fault interaction in the Eastern California shear zone: Geology, v. 29, p. 975–978, doi: 10.1130/0091-7613(2001)029<0975:TSAAFI>2.0.CO;2.

Rockwell, T.K., Lindvall, S., Herzberg, M., Murbach, D., Dawson, T., Berger, G., 2000, Paleoseismology of the Johnson Valley, Kickapoo, and Homestead Valley faults: Clustering of earthquakes in the eastern California shear zone: Bulletin of the Seismological Society of America, v. 90, p. 1200–1236, doi: 10.1785/0119990023.

Rubin, C and Sieh, K., 1997, Long dormancy, low slip rate, and similar slip-per-event for the Emerson fault, eastern California shear zone, J. Geophys. Res., v. 102, p. 15319-15333.

Sandwell, D.T., Sichoix, L., Agnew, D., Bock, Y., and Minster, J.-B., 2000, Geophysical Research Letters, Near real-time radar interferometry of the Mw 7.1 Hector Mine earthquake, v. 27, p. 3101–3104, doi: 10.1029/1999GL011209.

Spudich, P., and Olsen, K., 2001, Fault zone amplified waves as a possible seismic hazard along the Calaveras fault in Central California: Geophysical Research Letters, v. 28, p. 2533–2536, doi: 10.1029/2000GL011902.

Vidale, J.E., and Li, Y.-G., 2003, Damage to the shallow Landers fault from the nearby Hector Mine earthquake: Nature, v. 421, p. 524–526, doi: 10.1038/nature01354.

[1]GSA Data Repository item 2008xxx, xxxxxxxx, is available online at www.geosociety.org/pubs/ft2008.htm, or on request from editing@geosociety.org or Documents Secretary, GSA, P.O. Box 9140, Boulder, CO 80301, USA.

Data Repository:
Seismic and Geodetic Evidence For Extensive, Long-Lived Fault Damage Zones

Fault Zone Trapped Wave Data and Methods

Fault zone trapped waves observed on 2 shots and 5 local earthquakes (Table 1) are modeled using a 3D finite difference techniques. The data are low-pass filtered at 1, 2, or 3 Hz depending on the dominant period of the trapped waves. The model has a grid spacing of 0.0625 km. The parameters used to model the fault are: fault width is 1.5 km, the fault depth is 12 km, and shear-wave velocity reduction is 50%. Note that the low velocity zone is tapered linearly with depth giving an effective fault depth of about 5 km.

The depth of the low velocity zone is constrained by the deepest earthquake, local earthquake 200616317, which is located at an epicentral distance of 28 km and a depth of 11 km. Figure 1 shows a comparison of the data and synthetic waveforms computed for a LVZ that extends to 12 km depth and a low velocity zone that extends to only 3 km depth. It is clear that a 3 km deep LVZ does not sufficiently replicate the extended fault zone trapped waves observed in the data.

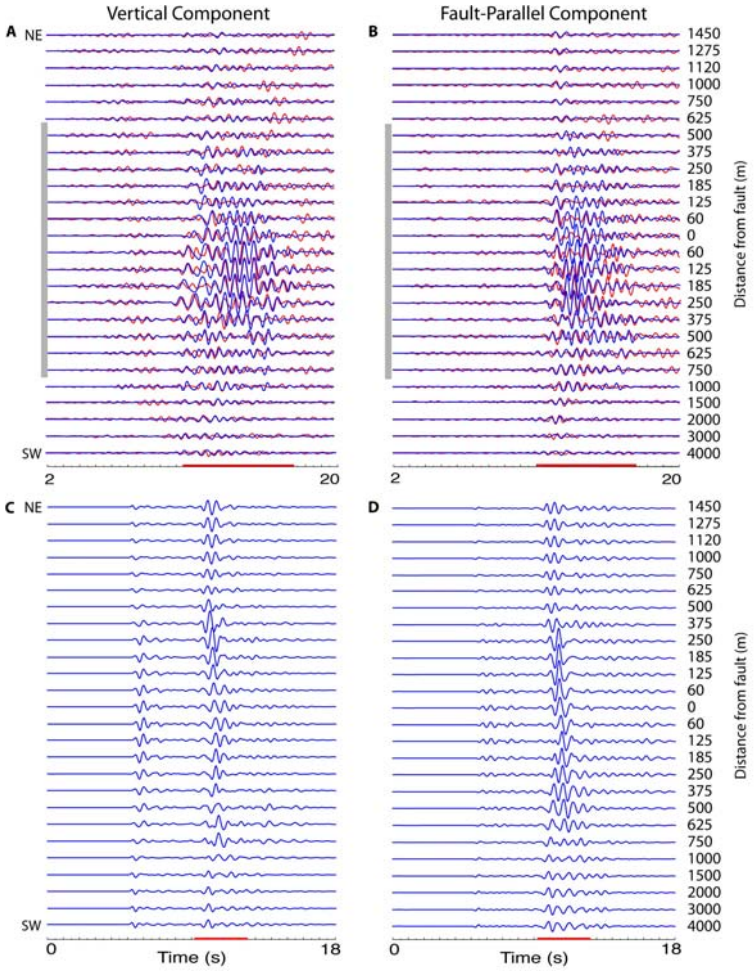

Figure 1. Fault Zone Trapped Wave Depth Dependence. Sensitivity of fault zone trapped waves to low velocity zone depth. **(A)** Actual (red) and synthetic (blue) vertical seismograms for local event 200616317. The red bar on the X-axis indicates the approximate location of the fault zone trapped waves. The width of the compliant zone is shown by the vertical grey bar on the Y-axis. Synthetic seismograms were computed using the model shown in Fig 4 and described in the text with a low velocity zone depth of 12 km. **(B)** Actual (red) and synthetic (blue) fault-parallel seismograms for local earthquake 200616317 **(C)** Actual (red) and synthetic (blue) vertical seismograms for local earthquake 200616317 for the same model as in (a) and (b) except with a low velocity zone depth of 3 km. (**D**) Actual (red) and synthetic (blue) fault-parallel seismograms for local earthquake 200616317 for the same model as in (a) and (b) except with a low velocity zone depth of 3 km. See Table 1 for location information. Data are low pass filtered at 2 Hz.

Travel Time Data and Methods

We use shots, local earthquakes, and teleseismic P-wave arrivals to model the fault zone properties (Table 2). The P-arrivals for the shots and local events were picked by hand as the arrivals were fairly impulsive and delay times were significant. Teleseismic P-wave arrivals were determined by cross-correlation. Figure 2 shows P arrivals for event 200627213 across line B, before and after cross-correlation delays are applied.

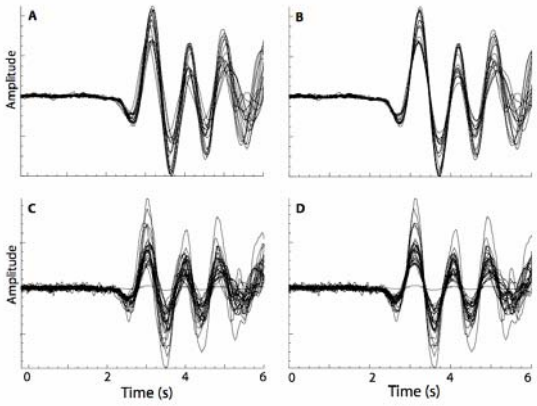

Figure 2. Travel Time Cross Correlation. Cross correlation of P-wave arrivals for teleseismic earthquake 200627213. **(A)** Intermediate period station (40T sensor) seismograms aligned using manual picks, **(B)** Intermediate period seismograms aligned using cross-correlation, **(C)** Short period station (L22 sensor) seismograms aligned using manual picks, **(D)** Short period seismograms aligned using cross-correlation.

To compute the travel times we use the graph theory technique of *Moser* (1991), modified as described in *Nolet et al.* (2005). Graph theory is based on the formulation of the shortest path through a network. Graph theory generates ray paths that are more accurate than traditional ray tracing methods and allows for unrestricted complexity or dimensionality of the velocity model. We model a range of fault parameters, modifying the velocity reduction, fault width, fault depth, and velocity taper across the fault and with depth. Fault width and velocity reduction are not fully independent, so slight variations in fault width and velocity reduction will give similar misfits. Figure 3 shows a comparison for different fault widths, given a velocity reduction of 40% and fault depth of 12 km. It is clear that fault widths less than 1 km do not fit the data well.

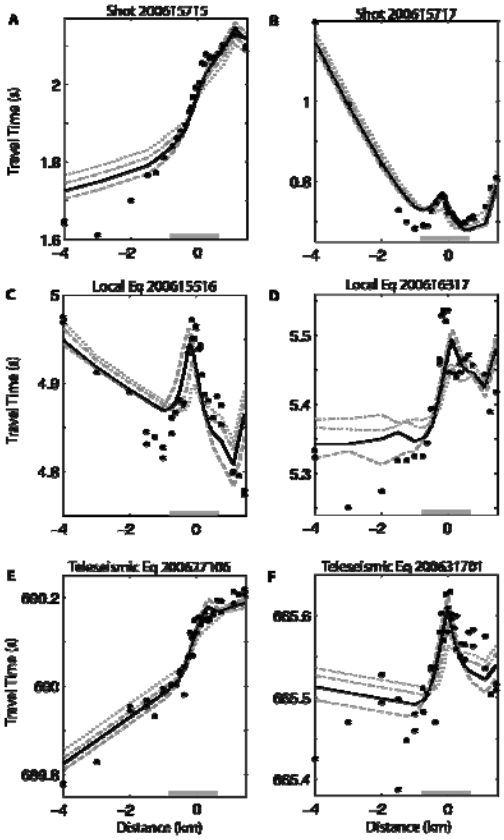

Figure 3. Low Velocity Zone Width Modeling. Predicted travel times for fault zone models with different low velocity zone widths (lines) to the actual travel times (points) across Line B. Velocity reduction is held constant at 40%. Models shown are 0.5 km wide low velocity zone, 1 km wide low velocity zone (dash-dot grey line), 1.5 km wide low velocity zone (solid black line), and 2 km wide low velocity zone (dashed grey line). Data are shown for events: **(A)** Shot 200615715, **(B)** Shot 200615717, **(C)** Local earthquake 200615516, **(D)** Local earthquake 200616317, **(E)** Teleseismic earthquake 200627106, and **(F)** Teleseismic earthquake 200631701. The approximate location of the low velocity zone is shown by the grey line along the X-axis. Event information can be found in Table 2.

Comparison of the InSAR and Seismic Data.

Models of permanent deformation due to coseismc stress changes allow us to constrain reduction in λ and μ, the Lamé parameters, within the fault zone, and directly compare the elastic structure that fits the InSAR data with the seismically inferred P-wave and S-wave velocities. The best fitting InSAR model has variations in the elastic properties assuming a Poisson solid, such that μ is reduced by 65% and λ is reduced by 30% within the fault zone. In terms of velocities, this would suggest a P-wave velocity reduction of about 30%

and an S-wave velocity reduction of 40%. Both the trapped wave data and the P-wave travel times suggest slightly higher velocity reductions within the low velocity zone, although the seismic data (fault zone trapped waves and travel times) do not constrain the velocities much better than ± 10%. We use an S-wave velocity reduction of 50% for the trapped wave synthetics and a velocity reduction of 40% to model the P-wave travel times. The geometries used to model the fault were the same in all three cases, with a fault width of 1.5 km and a fault depth of 12 km. The velocities are graded to background values away from the fault using a Hanning taper away from the fault slip plane and a linear taper with depth, as described in the main text.

Table 1. Fault Zone Trapped Wave Data. Distance is the epicentral distance in kilometers between the center of the seismic array (34.604, -116.477) and an event.

Event ID	Type	Magnitude	Latitude	Longitude	Depth	Distance
200615714	Shot	n/a	34.661	-116.536	0.0	8.4
200615717	Shot	n/a	34.597	-116.470	0.0	1.0
200616317	Local Earthquake	1.0	34.406	-116.290	10.8	27.9
200616813	Local Earthquake	1.1	34.587	-116.450	4.1	3.1
200626506	Local Earthquake	1.1	34.496	-116.349	3.4	16.8
200628602	Local Earthquake	1.5	34.876	-116.712	3.3	37.1
200632306	Local Earthquake	1.6	34.491	-116.328	3.2	18.6

Table 2. Travel Time Data. Distance is the epicentral distance between the center of the seismic array (34.604, -116.477) and an event. Distance is given in kilometers for shots and local earthquakes.

Event ID	Type	Magnitude	Latitude	Longitude	Depth	Distance
200615714	Shot	n/a	34.661	-116.536	0.0	8.4
200615715	Shot	n/a	34.635	-116.562	0.0	8.5
200615717	Shot	n/a	34.597	-116.470	0.0	1.0
200615511	Local Earthquake	1.4	34.816	-116.422	4.1	12.0
200615516	Local Earthquake	1.4	34.463	-116.234	8.1	27.2
200615621	Local Earthquake	1.0	34.488	-116.506	3.8	13.2
200615717	Local Earthquake	2.5	34.629	-116.657	6.4	16.7
200615721	Local Earthquake	1.2	34.705	-116.292	4.7	20.3
200616119	Local Earthquake	1.4	34.614	-116.667	8.2	17.4
200616317	Local Earthquake	1.0	34.406	-116.290	10.8	27.9
200618204	Local Earthquake	0.8	34.693	-116.330	12.0	16.7
200620405	Local Earthquake	1.3	34.506	-116.521	12.5	11.6
200620512	Local Earthquake	1.1	34.495	-116.461	11.2	12.2
200620803	Local Earthquake	1.2	34.780	-116.467	13.5	19.6
200620814	Local Earthquake	1.3	34.591	-116.629	8.1	14.0
200620819	Local Earthquake	1.9	34.444	-116.782	2.6	33.1
200621021	Local Earthquake	1.9	34.639	-116.665	6.3	17.7
200623307	Local Earthquake	1.2	34.550	-116.302	5.6	17.1
200626914	Local Earthquake	1.2	34.957	-116.536	3.2	39.7
200627905	Local Earthquake	1.1	34.767	-116.388	3.8	19.9
200628602	Local Earthquake	1.5	34.876	-116.712	3.3	37.1
200629617	Local Earthquake	1.5	34.468	-116.517	9.8	15.6
200630603	Local Earthquake	0.8	34.626	-116.203	15.8	25.2
200616918	Teleseism	5.9	32.970	-39.714	10.0	62.2°
200618920	Teleseism	6.6	51.259	-179.285	50.8	47.3°
200621818	Teleseism	5.8	26.091	144.035	23.1	82.7°
200624412	Teleseism	5.9	53.997	-166.366	78.1	39.5°
200627106	Teleseism	6.9	-16.613	-172.035	28.0	73.5°
200627213	Teleseism	6.1	10.910	-61.650	53.0	55.0°
200628817	Teleseism	6.7	19.878	-155.935	38.9	37.8°
200631701	Teleseism	6.8	-26.038	-63.243	547.5	78.9°